JOURNAL OF AIRCRAFT
Vol. 45, No. 3, May–June 2008

Comparison Study of Drag Prediction by Structured and Unstructured Mesh Method

Mitsuhiro Murayama* and Kazuomi Yamamoto†
Japan Aerospace Exploration Agency,
Chofu, Tokyo 182-8522, Japan

DOI: 10.2514/1.31072

Comparison study of computations for the Third AIAA Computational Fluid Dynamics Drag Prediction Workshop is performed on the DLR-F6 wing–body configurations with and without the wing–body fairing using the structured grid solver UPACS and unstructured grid solver TAS code. Grid convergence study at a fixed C_L using a family of three difference density grids and the results by α sweep are discussed. The self-made multiblock structured grids and mixed-element unstructured grids are employed. Another participant's grid is also compared. Comparisons between the two codes are conducted using the same turbulence model. Moreover, the detailed comparisons are conducted on the grid topology at the corner of the wing–body junction, the turbulence models, and the thin-layer approximation in viscous terms using the multiblock structured grids. The reconstruction schemes to realize the second-order spatial accuracy are also compared on unstructured grids. By comparing the results, the sensitivity of drag prediction to these factors is discussed.

Nomenclature

AR	=	wing aspect ratio
b	=	wing span
C_D	=	drag coefficient
C_{Df}	=	friction drag coefficient
C_{Dp}	=	pressure drag coefficient
C_f	=	skin friction coefficient
C_L	=	lift coefficient
C_M	=	pitching moment coefficient
C_p	=	surface pressure coefficient
c_{ref}	=	mean aerodynamic chord
M	=	Mach number
N	=	total number of grid point
p	=	pressure
Re	=	Reynolds number based on c_{ref}
S	=	reference area
$\hat{S}$	=	strain rate
T	=	temperature
α	=	angle of attack
γ	=	specific heat ratio
Δ	=	difference in quantity
ρ	=	density
χ	=	unstructured-MUSCL parameter
Ω	=	vorticity
∞	=	physical variables in freestream

I. Introduction

THE precise prediction of drag is important for a successful aerodynamic design of an aircraft. Especially, drag increments between configurations have to be well predicted in the design process. The reliability of drag prediction has been discussed in AIAA's computational fluid dynamics (CFD) drag prediction workshops (DPW) held by the AIAA Applied Aerodynamics Technical Committee. In the workshops, state-of-the-art computational methods solving Reynolds-averaged Navier–Stokes (RANS) equations have been assessed for aircraft force and moment prediction of industry relevant geometries. The first DPW (DPW-1) [1,2] was held in June 2001. In DPW-1, the DLR-F4 wing–body civil transonic aircraft configuration was employed. The results of DPW-1 showed an unexpected large scatter between CFD codes [1,2]. The second DPW (DPW-2) [3,4] was held in June 2003. In DPW-2, two DLR-F6 wing–body configurations with and without the nacelle-pylon were employed. The focus of the workshop was on drag prediction accuracy and component drag increments with/without the nacelle-pylon. The results of DPW-2 showed that the variation between CFD codes was reduced from DPW-1 and prediction of drag increment between configurations was better than that of the absolute value of drag, although still not at a desirable level [3,4]. The DLR-F6 wing–body configuration with the nacelle-pylon revealed large flow separations at the pylon by the strong interaction between the wing and the nacelle-pylon and at the corner of the wing–body junction. The flow separations had the possibility to spread the variation.

In the Third DPW (DPW-3)‡ [5,6] held in June 2006, two wing–body configurations with and without flow separation at the corner of the wing–body junction were employed to discuss how the flow separation affects the scatter. The DLR-F6 wing–body configurations were employed with and without a wing–body fairing, FX2B, which was designed to remove the boundary-layer separation at the wing–body junction [7]. In addition, a comparison study using two wing-alone configurations was also conducted for a simpler geometry without the flow separation to allow more grid convergence study.

This paper describes the computational work for DPW-3 using a structured grid solver, Unified Platform for Aerospace Computational Simulation (UPACS) and an unstructured grid solver, Tohoku University Aerodynamic Simulation code (TAS), by the Aviation Program Group in Japan Aerospace Exploration Agency (APG/JAXA). Additional work after the workshop is also included on the detailed comparison of turbulence models, viscous term approximation, and reconstruction scheme to realize the

Presented as Paper 258 at the 45th AIAA Aerospace Sciences Meeting and Exhibit, Reno, NV, 8–11 January 2007; received 16 March 2007; revision received 3 October 2007; accepted for publication 6 October 2007.

*Researcher, Civil Transport Team, Aviation Program Group. AIAA Member.

†Section Leader, Civil Transport Team, Aviation Program Group. AIAA Member.

‡http://aaac.larc.nasa.gov/tsab/cfdlarc/aiaa-dpw/ [cited 6 Jan. 2007]

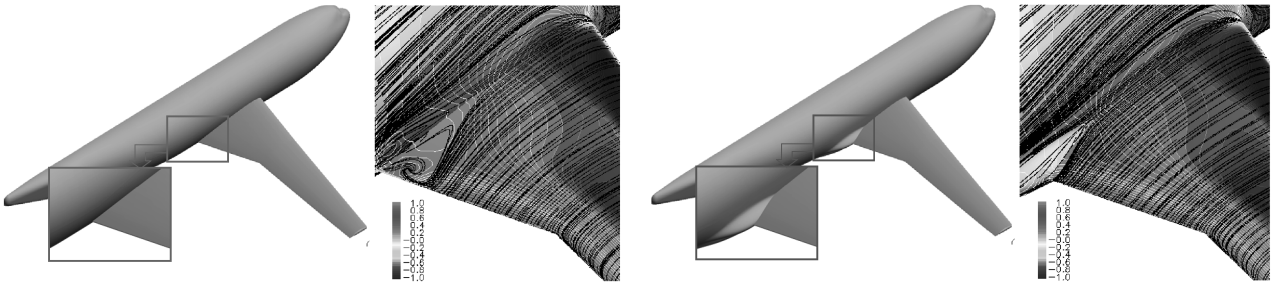

a) Without wing-body fairing (WB) b) With wing-body fairing (FX2B)

Fig. 1 DLR-F6 wing–body configuration.

second-order spatial accuracy on unstructured grids. In our study, the computations have been performed for two DLR-F6 wing–body configurations with and without the wing–body fairing. The self-made multiblock structured grids and mixed-element unstructured grids are used. The medium-size grid of the Boeing multiblock structured grids that are available on the DPW-3 Web site[‡] is also used only for the DLR-F6 wing–body configuration without the FX2B fairing.

Our results in DPW-2 [8] showed that the turbulence models, grid resolution at junction corners, and approximated computation in viscous terms affected the flow separation at the corner, and the factors had the possibility to result in the difference of drag prediction. Besides, our computational results on unstructured grids submitted to DPW-3 showed relatively larger grid dependency than our results on structured grids. Therefore, the following comparisons are performed and the computational results are validated: 1) comparison of the results by the difference of the reconstruction scheme on the JAXA unstructured grids; 2) comparison of the results on the JAXA multiblock structured and JAXA unstructured grids; 3) comparison of the results by the grid topology at the corner on the JAXA multiblock structured grids; 4) comparison of the results by turbulence models on the JAXA multiblock structured grids; 5) comparison of the results by the thin-layer approximation in viscous terms on the JAXA multiblock structured grids; 6) comparison of the results by the JAXA and Boeing multiblock structured grids. By comparing the results, this paper attempts to clarify the sensitivity of drag prediction to these factors.

II. Geometry Descriptions

In DPW-3[‡] [5,6], the computations are required on two configurations shown in Fig. 1: DLR-F6 wing-body configuration (WB) and DLR-F6 FX2B wing-body configuration with a wing–body fairing (FX2B). The DLR-F6 WB model represents a modern twin-engine transonic transport configuration [9]. The model was used in DPW-2 [3,4] and had a flow separation at the wing–body junction. The FX2B model has the addition of a wing–body fairing that was designed to remove the boundary-layer separation at the wing–body junction [7]. The CAD models are provided on the workshop Web site.[‡] The reference quantities are described in Table 1. The wind-tunnel test for the geometries at the computational conditions has not been conducted yet and the experimental data are not provided.

Table 1 Reference quantities for the DLR-F6 wing–body configuration

Reference quantities	
Half-model reference area, $S/2$	72,700 mm^2
Mean aerodynamic chord, c_{ref}	141.2 mm
Moment reference from fuselage nose	$\Delta x = 504.9$ mm, $\Delta z = -51.42$ mm (aft and below nose)
Projected half-span, $b/2$	585.647 mm
Aspect ratio, AR	9.5 (9.436)

III. Computational Conditions

For the DLR-F6 wing–body configurations with and without the FX2B fairing, grid convergence study at $C_L = 0.500\,(\pm 0.001)$ using three difference density (coarse, medium, and fine) grids and drag polar at $\alpha = -3.0, -2.0, -1.0, -0.5, 0.0, 0.5, 1.0, 1.5$ using the medium-size grids are required. For all cases, M_∞ is 0.75, Re is 5×10^6, and T_∞ is 322.22 K. A fully turbulent boundary layer is assumed in the computations. In DPW-2, the experimental Re is 3 million. In DPW-3, Re is increased to 5 million to reduce the flow separation near the wing trailing edge.

IV. Computational Method

A. Multiblock Structured Grid Solver: UPACS

As the flow solver on multiblock structured grids, UPACS is used, which is a standard CFD code for multiblock structured grids in Japan Aerospace Exploration Agency [8,10,11]. The flow solver is based on a cell-centered finite volume method. It is collaborative computational software designed to be shared among researchers. Besides the flexibility and extendibility, the reliability is especially emphasized in its development. In this study, the second-order scheme of the Roe's flux difference splitting for convection terms [12] is used with MUSCL extrapolation and van Albada's limiter [13]. The viscous terms are discretized using a scheme based on the second-order central difference. Both full- and thin-layer approximation Navier–Stokes equations are implemented. In the thin-layer approximation, the cross terms in the viscous flux terms are omitted. The approximation is also applied to the equations for the turbulence models. Most of the calculations were performed with full Navier–Stokes equations. The time integration is carried out using the Matrix Free Gauss–Seidel (MFGS) implicit method [14].

B. Unstructured Grid Solver: TAS Code

As the unstructured grid generator and flow solver, TAS code [15] is used in this study. TAS_Flow is the flow solver. In TAS_Flow, full Navier–Stokes equations are solved on the unstructured grid by a cell-vertex finite volume method. The Harten–Lax–van Leer–Einfeldt–Wada (HLLEW) method [16] is used for the numerical flux computations. The Lower/Upper Symmetric Gauss–Seidel (LU-SGS) implicit method [17] is used for the time integration.

Second-order spatial accuracy is realized by a linear reconstruction of the primitive variables with Venkatakrishnan's limiter [18] in our computational results submitted to DPW-3 held in June 2006. To discuss the effect on the drag prediction by the reconstruction scheme, the unstructured-MUSCL scheme (U-MUSCL) [19] is introduced:

$$\tilde{Q}^{L}_{i+1/2} = Q_i + \frac{\chi}{2}(Q_{i+1} - Q_i) + (1-\chi)\nabla Q_i \cdot \frac{\hat{r}}{2} \qquad (1)$$

where Q, ∇Q, $\hat{r}$, and χ are variables, gradient of Q, vector between nodes, and U-MUSCL parameter, respectively. The original reconstruction scheme is given by $\chi = 0$. In this study, χ is 0.5. For the computation of the gradients of variables, the Green–Gauss method is used in both reconstruction schemes.

Table 2 Summary of computational methods used in UPACS and TAS

	UPACS	TAS
Mesh type	multiblock structured	mixed element unstructured
Governing equations	full-NS/thin-layer NS	full-NS
Discretization	cell-centered finite volume	cell-vertex finite volume
Flux computation	Roe second order [12]	HLLEW second order [16]
Limiter in flux computation	van Albada [13]	Venkatakrishnan [18]
Time integration	MFGS [14]	LU-SGS [17]
Turbulence model	SA_model [20,22,23], SST [21]	SA_model

C. Turbulence Models

Two turbulence models, the Spalart–Allmaras one-equation model (SA) [20] and Menter's shear stress transport k-ω two-equation model (SST) [21], are compared. In the study, the SA model is used as a standard model.

The equations for the turbulence models are also solved using the second-order scheme in both UPACS and TAS. Both UPACS and TAS employ the SA model without the trip term for transition and the $ft2$ function, which serves to suppress the production of eddy viscosity due to numerical error. The production of eddy viscosity starts with the freestream value. A variation of the model, which reduces the eddy viscosity in the regions of high vorticity [22,23], is used. In this study, a simple combination using the minimum of the vorticity $\Omega = \sqrt{2\Omega_{ij}\Omega_{ij}}$ and strain rate $\hat{S} = \sqrt{2s_{ij}s_{ij}}$ is used in the modification [23] as follows:

$$S = \Omega + C_{\text{vor}} \min(0, \hat{S} - \Omega) \tag{2}$$

Here, $C_{\text{vor}} = 1$ for the present computations. The modified model computes turbulent vortical flow without adding much dissipation to the vortex core.

The computational methods used in UPACS and TAS are summarized in Table 2.

D. Computing Platform

Computations were carried out on the Fujitsu PRIMEPOWER HPC2500 multiprocessor (SPARC 64V, 1.3 GHz, 1792 CPU), which is the main machine of the Numerical Simulator III system in the Japan Aerospace Exploration Agency [24]. Although the required CPU time to get converged solutions varied depending on the angles of attack and the flowfields with/without the flow separation, the converged results on the fine grids of the WB configuration without FX2B required 71 h for the fine structured grids (29.8 million grid points) using 100 CPUs and 75 h for the fine unstructured grid (17.5 million grid points) using 64 CPUs.

V. Computational Grids

The multiblock structured grids and mixed-element unstructured grids were generated according to DPW-3 gridding guidelines on the DPW-3 Web site.[‡] A grid family with three levels of density (coarse, medium, and fine) is required. The gridding guideline describes the total grid size, far-field boundary location ($\sim 100 c_{\text{ref}}$), chordwise spacing at wing leading edge and trailing edge ($\sim$0.1% local chord on the medium grid), wing spanwise spacing at root and tip ($\sim$0.1% semispan on the medium grid), cell size near the fuselage nose and afterbody ($\sim 2.0\% c_{\text{ref}}$ on the medium grid), spacing normal to viscous walls, growth rate of cell sizes (<1.25), and the number of cells on the wing trailing-edge base. Most of the results presented in this paper were obtained on the self-made grids. Besides the self-made grids, the medium-size grid of the Boeing multiblock structured grids that are available on the DPW-3 Web site[‡] was also used only for the DLR-F6 wing–body configuration without the FX2B fairing.

A. JAXA Multiblock Structured Grids

The multiblock structured one-to-one point-matched grids for UPACS were generated with commercial software, Gridgen. Near the model surface, the grid wraps around the configuration basically with O—O grid topology to guarantee good orthogonality within the boundary layer, and then extends outward with C—O topology. The medium grid is shown in Fig. 2. At the corner of the wing–body junction, two kinds of grid topologies are used, as shown in Fig. 3. The grid "simple type" in Fig. 3a was generated by inserting a block to keep good orthogonality at the corner. The grid "extrude type" in Fig. 3b was generated by extruding the boundary-layer grid normal to the wing and body, and averaging the normal vector. In the study, simple-type grid topology is used as a standard grid.

Figures 4–6 show the close-up and cross-sectional views of the surface and volume grids. Information of the multiblock structured grids is summarized in Table 3 and 4.

B. JAXA Mixed-Element Unstructured Grids

The mixed-element unstructured grids composed of tetrahedrons, prisms, and pyramids for viscous flows with high Reynolds number were generated using an unstructured surface/volume mesh generator, Edge-Editor in TAS-Mesh [25–29]. Edge-Editor is a mesh generator with graphical user interface tools. The surface grids are triangulated with the direct advancing front method using stereolithography (STL) files as background grids for the surface definition [25,26]. As the mixed-element volume grid generation method for viscous flows with high Reynolds number, two approaches can be selected: 1) After the tetrahedral meshing

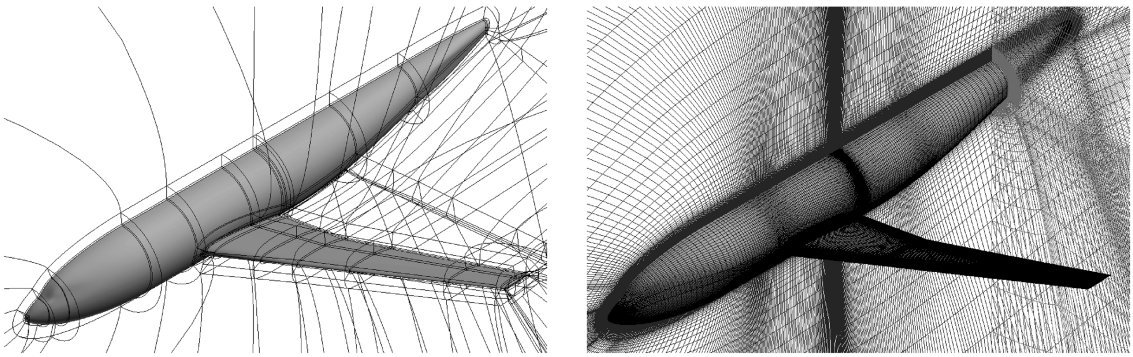

a) Wire frame **b) Generated multiblock structured grid**

Fig. 2 JAXA multiblock structured grid for the WB configuration (medium grid).

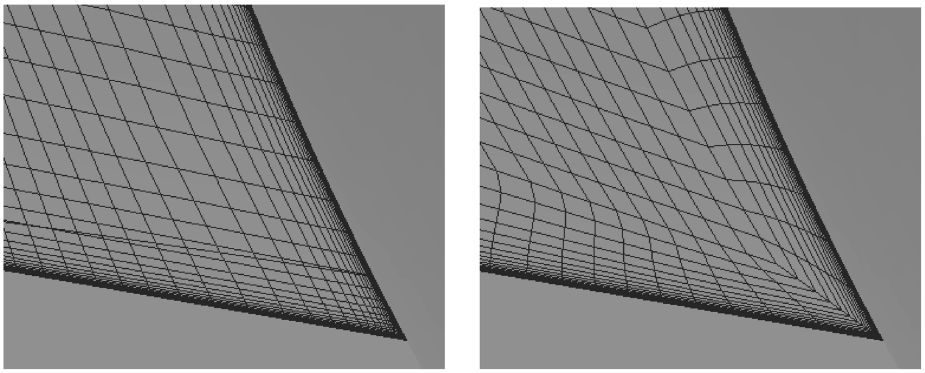

a) Simple type b) Extrude type

Fig. 3 Grid topology at the corner of the wing–body junction for the structured grids.

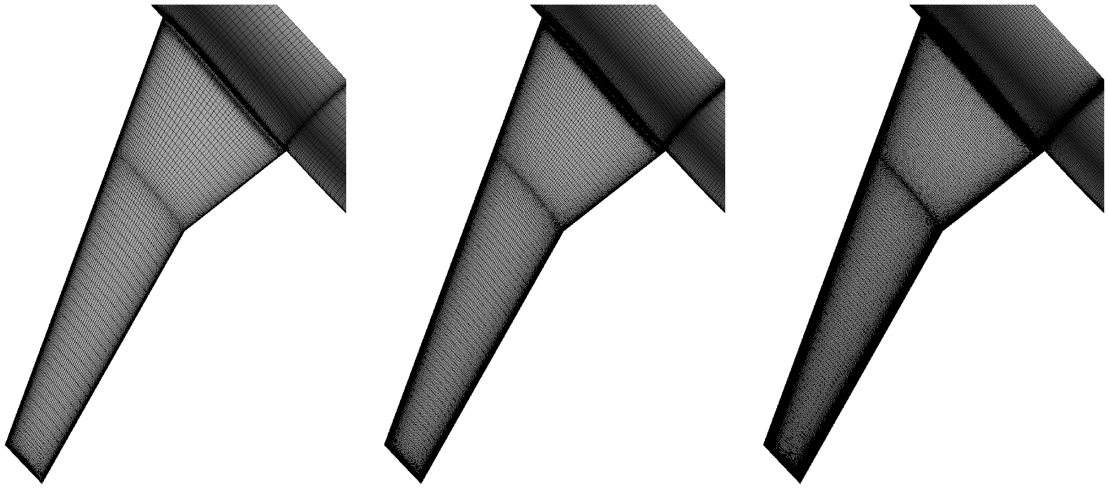

a) Distant view of the surface grids

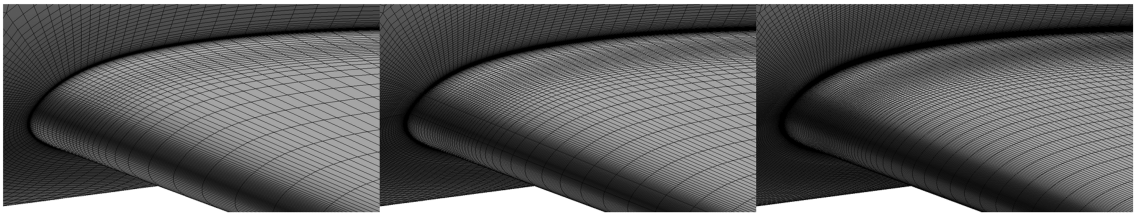

b) Close-up view of the surface grids near the leading edge at the wing-body junction

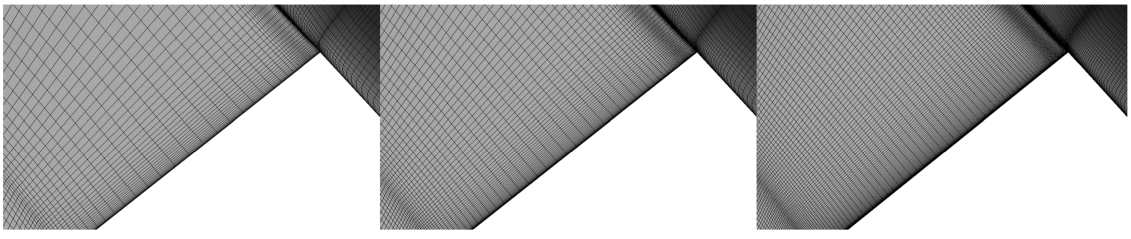

c) Close-up view of the surface grids near the trailing edge at the wing-body junction

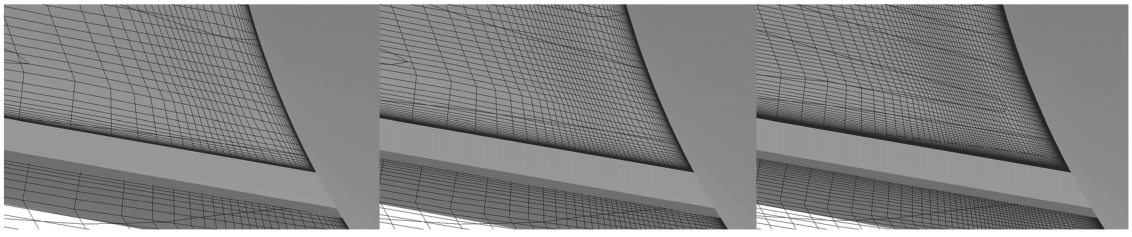

d) Cross-sectional view near the trailing edge at the wing-body junction

Fig. 4 Close-up views of the JAXA multiblock structured grids for the WB configuration (simple-type corner grid); left: coarse grid, center: medium grid, right: fine grid.

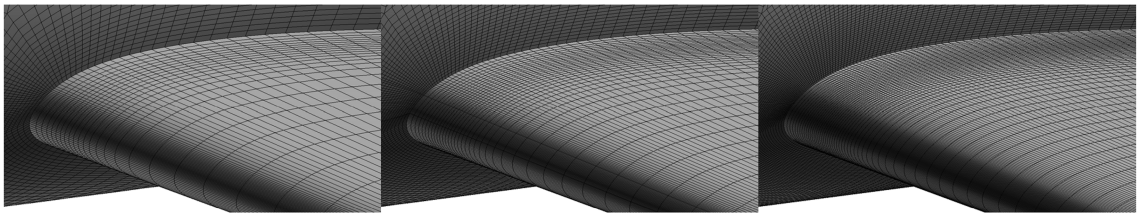

a) Close-up view of the surface grids near the leading edge at the wing-body junction

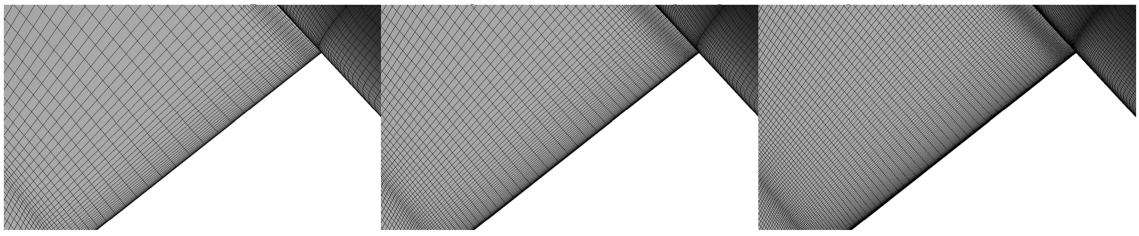

b) Close-up view of the surface grids near the trailing edge at the wing-body junction

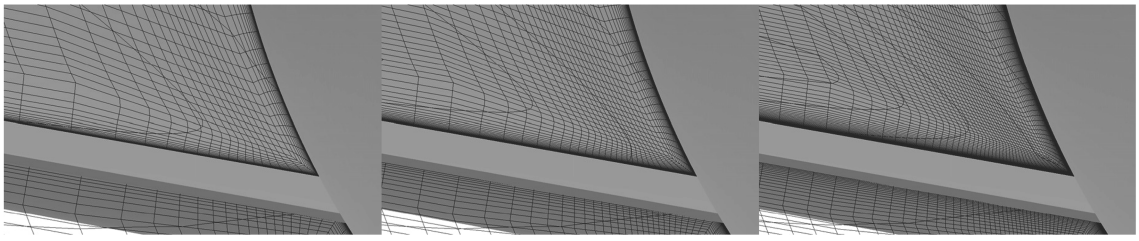

c) Cross-sectional view near the trailing edge at the wing-body junction

Fig. 5 Close-up views of the JAXA multiblock structured grids for the WB configuration (extrude-type corner grid); left: coarse grid, center: medium grid, right: fine grid.

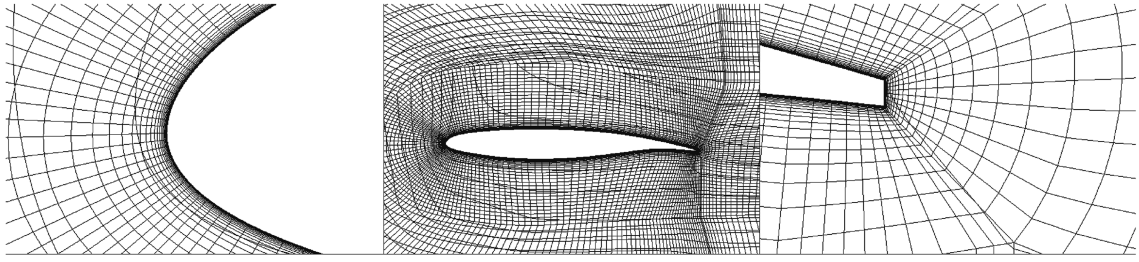

a) Coarse grid

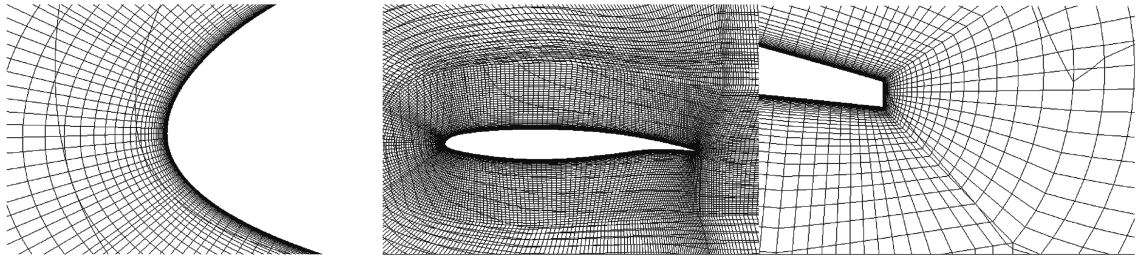

b) Medium grid

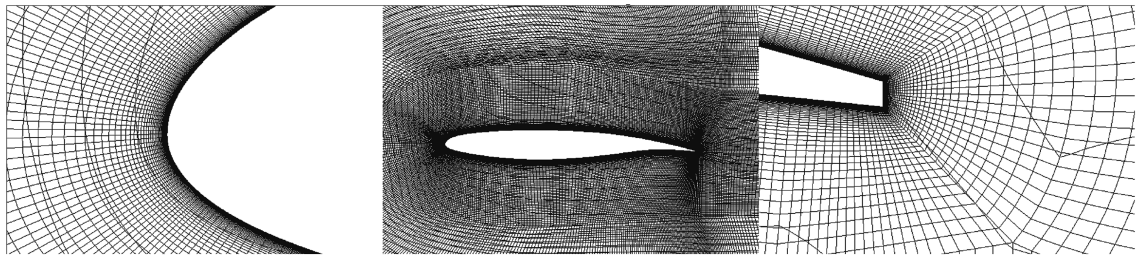

c) Fine grid

Fig. 6 Cross-sectional views at the kink of the JAXA multiblock structured grids for the WB configuration (simple-type corner grid).

Table 3 Summary of the JAXA multiblock structured grids (simple-type corner grid)

Configuration	Grid density	Number of nodes (volume grid)	Number of nodes (surface grid)	First grid cell size	Growth rate	Number of cells on trailing edge (TE)
DLR-F6 WB	coarse	3.1 million	47 K	6.0×10^{-4}, mm	1.29	8
	medium	9.8 million	100 K	4.0×10^{-4}, mm	1.17	12
	fine	29.8 million	209 K	2.7×10^{-4}, mm	1.12	16
DLR-F6 FX2B	coarse	3.3 million	49 K	6.0×10^{-4}, mm	1.29	8
	medium	10.0 million	103 K	4.0×10^{-4}, mm	1.17	12
	fine	29.3 million	209 K	2.7×10^{-4}, mm	1.12	16

Table 4 Summary of the JAXA multiblock structured grids (extrude-type corner grid)

Configuration	Grid density	Number of nodes (volume grid)	Number of nodes (surface grid)	First grid cell size	Growth rate	Number of cells on TE
DLR-F6 WB	coarse	3.0 million	47 K	6.0×10^{-4}, mm	1.29	8
	medium	9.3 million	100 K	4.0×10^{-4}, mm	1.17	12
	fine	28.4 million	209 K	2.7×10^{-4}, mm	1.12	16
DLR-F6 FX2B	coarse	3.0 million	49 K	6.0×10^{-4}, mm	1.29	8
	medium	9.3 million	103 K	4.0×10^{-4}, mm	1.17	12
	fine	28.4 million	209 K	2.7×10^{-4}, mm	1.12	16

(Delaunay or advancing front method), prismatic layers for the boundary layer are inserted [28]; 2) After the generation of prismatic layers for the boundary layer, the advancing front method is used as the tetrahedral meshing [29]. In this study, the former approach is used. The mixed-element volume grid generation starts with the isotropic tetrahedral grid generation to enhance the robustness. The isotropic tetrahedral volume grids are generated using the method of Delaunay tetrahedral meshing [27]. Then, prismatic layers are added on the nonslip walls, while the tetrahedral elements near the nonslip walls are shifted inward by a Laplacian-like method [28]. The addition of the prism layers is locally stopped if negative volume elements are created. At the corner of the wing–body junction, the extrude-type grid is used. The medium grid is shown in Fig. 7.

A grid family with three levels of density (coarse, medium, and fine) was generated according to DPW-3 gridding guidelines. However, the guideline for the minimum grid resolution on the wing trailing-edge base was not kept. The unstructured surface meshing using nearly isotropic triangles in this study is semi-automatic. However, a huge number of mesh points are necessary to insert grid points required in the guideline using the nearly isotropic triangles on the thin trailing-edge base. On the present unstructured grids, 4, 5, and 6 cells were placed on the trailing edge for coarse, medium, and fine grids, respectively, although 8, 12, and 16 cells should be placed according to the gridding guideline. Figures 8 and 9 show the close-up and cross-sectional views of the surface and volume grids. Information of the unstructured grids is summarized in Table 5.

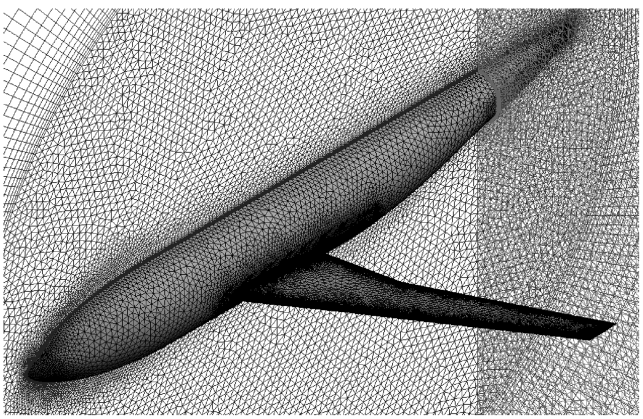

Fig. 7 JAXA mixed-element unstructured grid for the WB configuration (medium grid).

C. Boeing Multiblock Structured Grids

The Boeing multiblock structured one-to-one point-matched grids are available on the DPW-3 Web site.[‡] In this study, only the medium grid for the DLR-F6 WB configuration shown in Fig. 10 is used. A H–H grid topology is used and the number of the blocks is five. The base of the blunt trailing edge and the tip face of the wing are treated as inviscid surfaces due to the use of the grid, which is not adequate to resolve the viscous layer. The number of the grid points is 9.2 million on the medium grid. At the corner of the wing–body junction, the extrude-type grid is used. Detailed information of the grid is in [30].[‡] Figures 11 and 12 show the close-up and cross-sectional views of the surface and volume grids.

VI. Results

A. Comparison by the Difference of the Reconstruction Scheme on JAXA Unstructured Grids

To discuss the effect on the drag prediction by the reconstruction scheme on the unstructured grids, the original linear reconstruction scheme [$\chi = 0$ in Eq. (1)] and U-MUSCL scheme [$\chi = 0.5$ in Eq. (1)] are compared.

Richardson extrapolation is used to evaluate the grid convergence of the drag. Figure 13 shows plots of C_D and C_{Df} at fixed $C_L = 0.5$ vs a function of $N^{-2/3}$. The $N^{-2/3}$ is based on the second-order accuracy of the numerical method. Zero value of $N^{-2/3}$ means the infinite grid size. For the second-order accurate method using a family of uniformly refined grids, the results should be arranged on a straight line and the value on an infinite grid size can be extrapolated.

Regarding the FX2B configuration, both results show good linear grid convergence, although they do not seem to be converged even on the fine grid. The gradients of the grid convergence are different, whereas the values on the infinite grid size are the same, 262 cts. (1 cts. = 0.0001). The gradient using the U-MUSCL scheme is smaller and the grid dependency is decreased. On the coarse grid, C_D is reduced by 10 drag cts. when the U-MUSCL scheme is employed. Regarding the WB configuration, the fold of the grid convergence is observed on the results using the linear reconstruction scheme, whereas the results using the U-MUSCL scheme show similar grid convergence with the results of the FX2B configuration and decrease of the grid dependency. Regarding the friction drag shown in Fig. 13b, the change with the grid size and scheme is small and the difference is within 1 cts.

In Figs. 14 and 15, C_p distributions at 15 and 41% span locations on each density grid for the WB configuration are compared. The results using the U-MUSCL scheme resolve the shock wave more clearly and show less grid dependency for the shock wave.

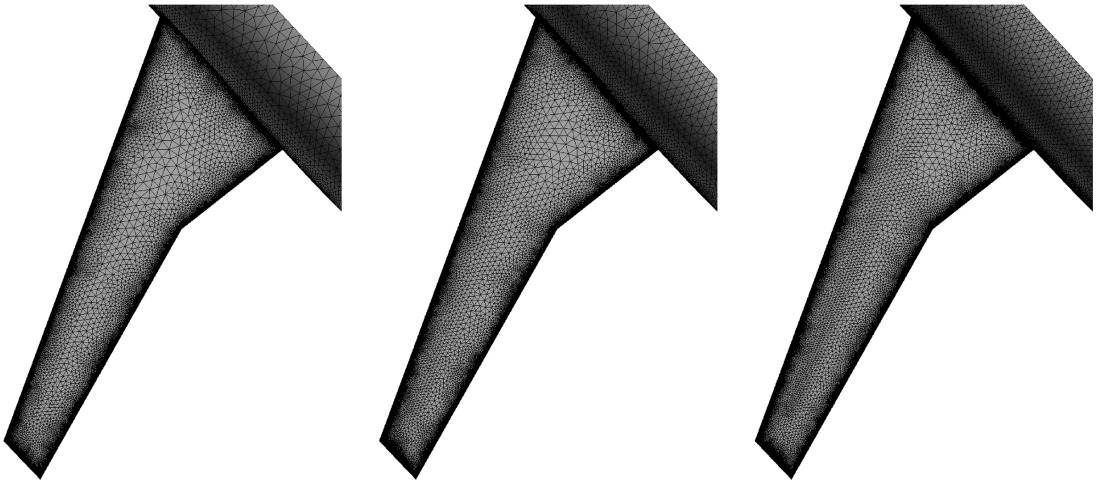

a) Distant view of the surface grids

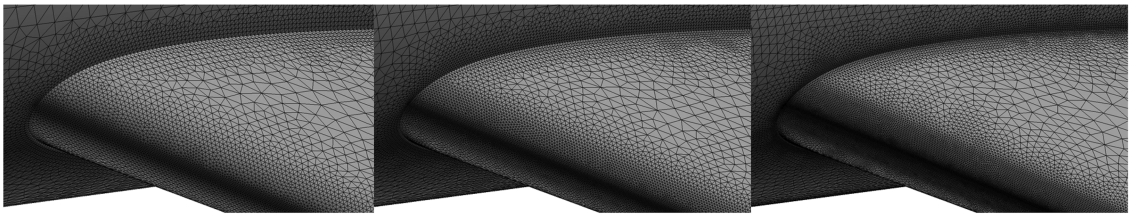

b) Close-up view of the surface grids near the leading edge at the wing-body junction

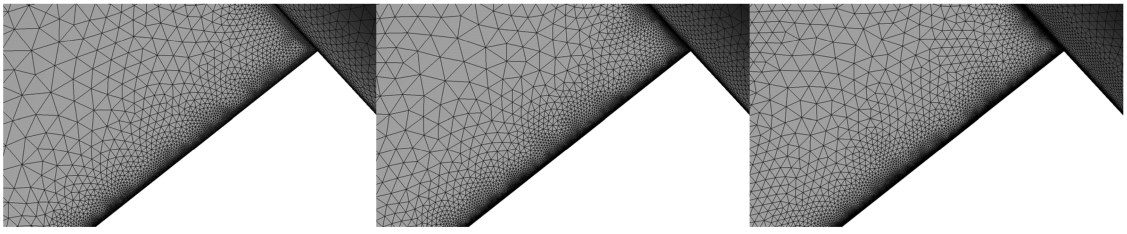

c) Close-up view of the surface grids near the trailing edge at the wing-body junction

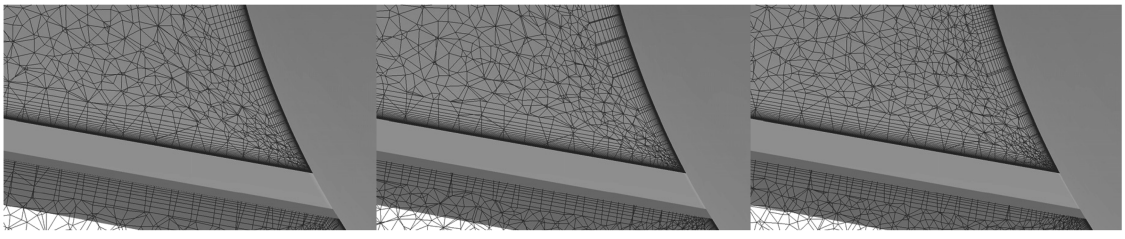

d) Cross-sectional view near the trailing edge at the wing-body junction

Fig. 8 Close-up views of the JAXA mixed-element unstructured grids for the WB configuration; left: coarse grid, center: medium grid, right: fine grid.

Figures 16 and 17 show the contours of entropy change, which is defined as follows:

$$\frac{\Delta s}{R} = \frac{1}{\gamma - 1} \ell_n \left[\frac{p}{p_\infty} \left(\frac{\rho_\infty}{\rho} \right)^\gamma \right] \tag{3}$$

The contours in the figures are visualized using narrow range from 10^{-6} to 10^{-3}. In general, the entropy increment can be observed in the boundary layers and after the generation of shock waves. In Figs. 16 and 17, the entropy is nonphysically increased in the regions near the leading edge and away from the wing surface by the numerical errors, which indicates insufficient resolution. The nonphysical entropy increment is decreased on finer grids. Comparing the results shown in Figs. 16 and 17, the results using the U-MUSCL scheme show much less numerical errors. The decrease of the numerical dissipation results in the improvement of the resolution for shock wave and the lower drag.

B. Comparison on JAXA Multiblock Structured Grids and JAXA Unstructured Grids

The results on the JAXA multiblock structured grids (simple-type corner grid) and JAXA unstructured grids are compared. The full Navier–Stokes equations are solved in both codes. The same SA turbulence model is used.

Figure 18 shows the solution convergence histories obtained on the medium grids for the WB configuration at a fixed $\alpha = 0.5$ deg. The computations are restarted from the results at lower $\alpha = 0.0$ deg. Both histories by UPACS and TAS show good convergence, although the WB configuration model has flow separation at the wing–body junction as shown in Fig. 1a. C_D is fully converged at below 1 drag cts. or less. The other computational results at the other angles of attack and on the coarse and fine grids show similar solution convergence histories.

Figure 19 shows the plots of the grid convergence of C_D and C_{Df} at fixed $C_L = 0.5$. Angles of attack to keep $C_L = 0.5$ are plotted in

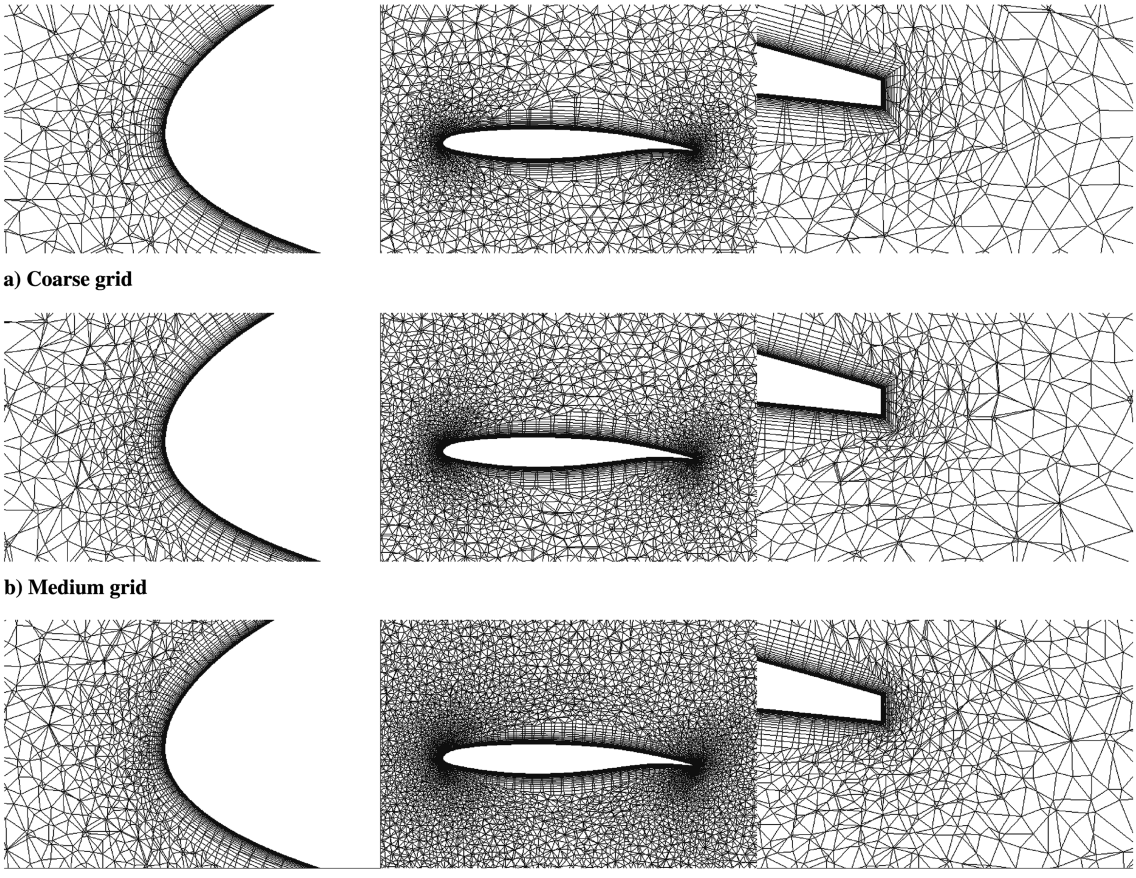

a) Coarse grid

b) Medium grid

c) Fine grid

Fig. 9 Cross-sectional views at the kink of the JAXA mixed-element unstructured grids for the WB configuration.

Fig. 19c. The results by UPACS show good linear grid convergence and similar gradients for both configurations. Comparing the results by UPACS and TAS, the gradients of the grid convergence are different, whereas the values on the infinite grid size are nearly the same: $262 \sim 263$ cts. for the FX2B configuration and $277 \sim 278$ cts. for the WB configuration. The gradients of the grid convergence by UPACS are smaller. On the medium grids, the difference between UPACS and TAS, $\Delta C_{D(\mathrm{TAS})-(\mathrm{UPACS})}$, is about $+4$ drag cts. for the FX2B configuration and $+1$ drag cts. for the WB configuration. Regarding the friction drag, the change with the grid size is small in both codes and the difference is within 1 cts. Both codes can similarly predict the difference of the friction drag between two configurations, $\Delta C_{Df(\mathrm{WB})-(\mathrm{FX2B})}$. Figure 20 shows the plot of the grid convergence of $\Delta C_{D(\mathrm{WB})-(\mathrm{FX2B})}$. TAS shows relatively larger grid dependency for $\Delta C_{D(\mathrm{WB})-(\mathrm{FX2B})}$, whereas $\Delta C_{D(\mathrm{WB})-(\mathrm{FX2B})}$ on the infinite grid size by both codes are similar: $+14.5$ cts for UPACS and $+16$ cts. for TAS. The angles of attack are different between UPACS and TAS, whereas the direction of the change and $\Delta\alpha$ to keep $C_L = 0.5$ agree well when the geometry is changed from the WB configuration to the FX2B configuration.

Figures 21 and 22 show the computed oil flows and C_p near the wing–body junction for the WB configuration by TAS and UPACS. The separation bubbles are visualized on the wing and body. The size of the separation bubbles does not change largely on each grid density. The size by UPACS is a little larger than that by TAS. Larger separation bubble leads to larger pressure drag. The small difference of the separation bubbles seems to reveal $\Delta C_{D(\mathrm{TAS})-(\mathrm{UPACS})}$ for the WB configuration.

Figures 23 and 24 show the plots of the grid convergence of C_D, C_{Dp}, and C_{Df} on the wing and body. The gradients of the grid convergence and the drag values on the infinite grid size agree well on the wing in both codes. On the other hand, there is a difference of the gradients of C_D on the body, although the drag values on the finite grid size and $\Delta C_{D(\mathrm{WB})-(\mathrm{FX2B})}$ agree well. The difference derives from the pressure drag shown in Fig. 24b. The TAS results for C_{Dp} show larger gradients on the body, which indicates larger grid dependency. These results show that the relatively larger grid dependency of the total drag on the unstructured grids comes from insufficient grid resolution of the body on the coarse and medium grids. The grid density of the coarse unstructured grid on the body is much coarser

Table 5 Summary of the JAXA mixed-element unstructured grids

Configuration	Grid density	Number of nodes (volume grid)	Number of nodes (surface grid)	First grid cell size	Growth rate	Number of cells on TE
DLR-F6 WB	coarse	5.4 million	134 K	6.0×10^{-4}, mm	1.20	4
	medium	9.4 million	219 K	4.0×10^{-4}, mm	1.20	5
	fine	17.5 million	368 K	2.7×10^{-4}, mm	1.20	6
DLR-F6 FX2B	coarse	5.4 million	136 K	6.0×10^{-4}, mm	1.20	4
	medium	9.5 million	223 K	4.0×10^{-4}, mm	1.20	5
	fine	17.2 million	378 K	2.7×10^{-4}, mm	1.20	6

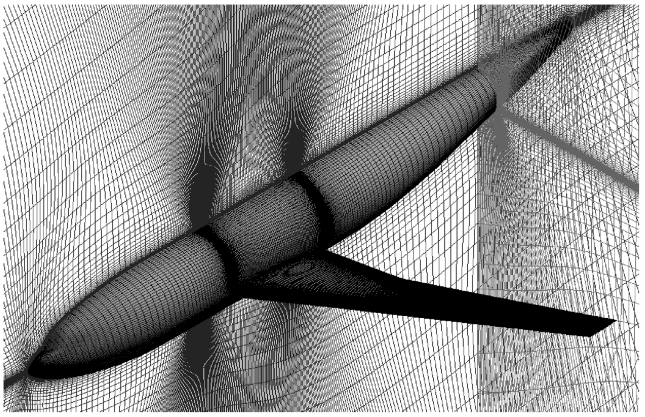

Fig. 10 Boeing multiblock structured grid for the WB configuration (medium grid).

than that of the structured grid, as shown in Figs. 4 and 8. More experienced gridding guidelines will be required on the body for our unstructured grids.

Figure 25 compares C_L-α on the medium grids. Regarding C_L-α, both codes show good agreement in the slope although there are small shifts of C_L by 0.01 for the WB configuration and 0.02 for the FX2B configuration. Figure 26 compares C_L-C_D and C_L-C_{Df} on the medium grids. Both codes show good agreement in the polar curves for both configurations even at lower and higher C_L, and the increment by the geometry change is also consistent. Figure 27 compares C_L-C_M on the medium grids and the grid dependency of C_L-C_M for the FX2B configuration. $\Delta C_{M(\mathrm{WB})-(\mathrm{FX2B})}$ is consistent in both codes, whereas shifts of C_M are also observed between the codes. As shown in Fig. 27b, the grid dependency on the unstructured grids is larger. By the increase of the grid resolution, TAS shows better agreement with UPACS. Figure 28 shows C_p distributions by UPACS at 15 and 41% span locations for the WB configuration. Compared with the results by TAS shown in Fig. 15, the UPACS results show less grid dependency even for the separation near the wing–body junction. In addition, the UPACS results show much smaller C_p jump near the trailing edge. On the unstructured grids, as shown in Figs. 8 and 9, the volume grids are not uniformly refined in space and the grid resolution in space away from the wing surface is lower, because the change of the number of the grid points is mainly adjusted by the surface grid density and less number of grid points are placed on the trailing-edge base of unstructured grids than that of structured grids, as explained in Sec. V.B.

Next, the grid dependency study for the flow separation near the wing trailing edge was performed on the FX2B configuration. In DPW-2, the results by the unstructured grids had a tendency to predict the trailing-edge separation, which appeared in the flow visualization by the wind-tunnel experimental result. However, many results by structured grids including UPACS did not predict. In DPW-3, Re is increased to 5 million to reduce the region of the wing trailing-edge separation, whereas the results by TAS showed subtle trailing-edge separation regions, as shown in Fig. 29. Figure 29 shows the oil-flow patterns near the kink trailing edge at $C_L = 0.5$ on each grid density. The trailing-edge separation decreases with the grid refinement from the coarse grid to the fine grid. As shown in Fig. 19c, the angles of attack to keep $C_L = 0.5$ are also decreased with the grid refinement. Figure 30 shows the oil-flow patterns at $\alpha = -0.5$ and 0.5 on the medium grid and at $\alpha = 0.5$ on the fine grid.

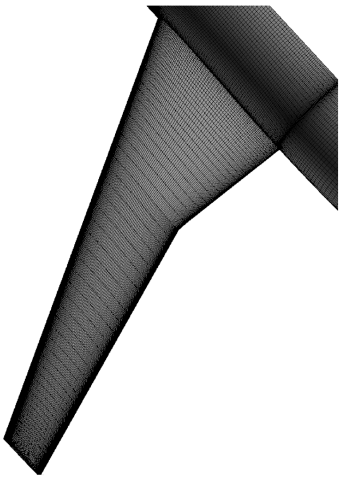

a) Distant view of the surface grids

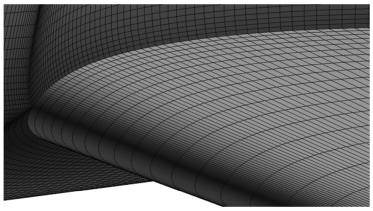

b) Close-up view of the surface grids near the leading edge at the wing-body junction

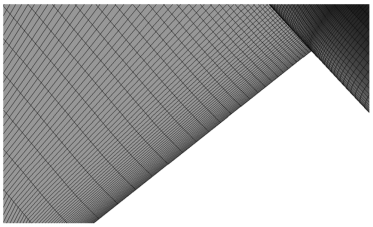

c) Close-up view of the surface grids near the trailing edge at the wing-body junction

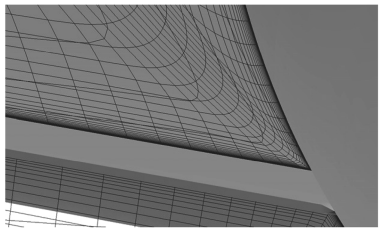

d) Cross-sectional view near the trailing edge at the wing-body junction

Fig. 11 Close-up views of the Boeing multiblock structured grid for the WB configuration (medium grid).

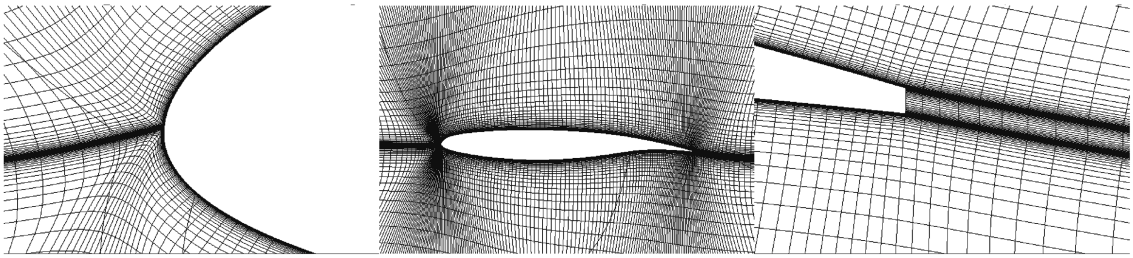

a) Cross-sectional views at the kink of the Boeing multi-block structured grid for the WB configuration (Medium grid)

Fig. 12 Cross-sectional views at the kink of the Boeing multiblock structured grid for the WB configuration (medium grid).

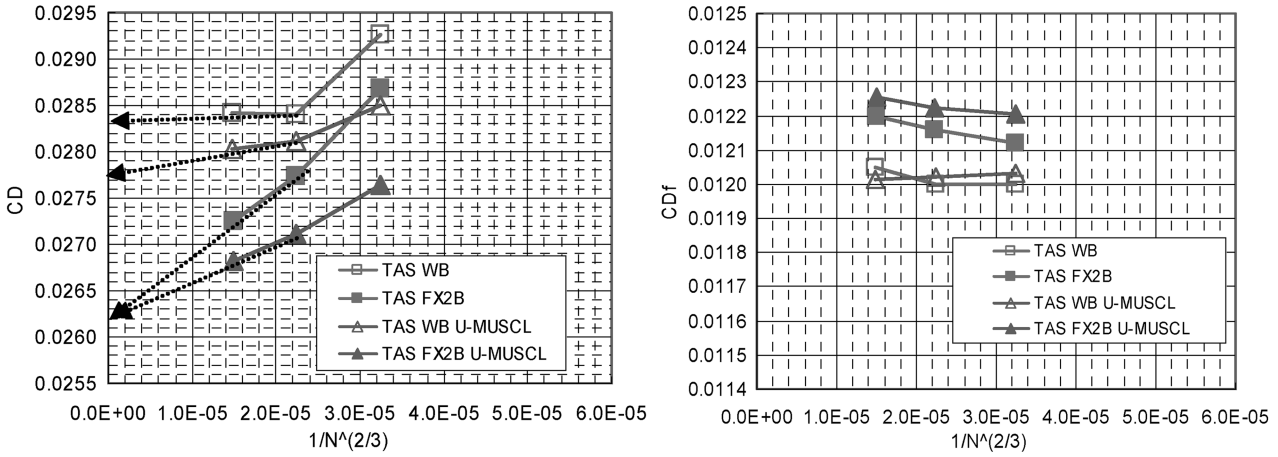

a) C_D **b)** C_{Df}

Fig. 13 Comparison of the grid convergence of C_D and C_{Df} at $C_L = 0.5$ by the reconstruction schemes on the unstructured grids (TAS, full-NS, SA).

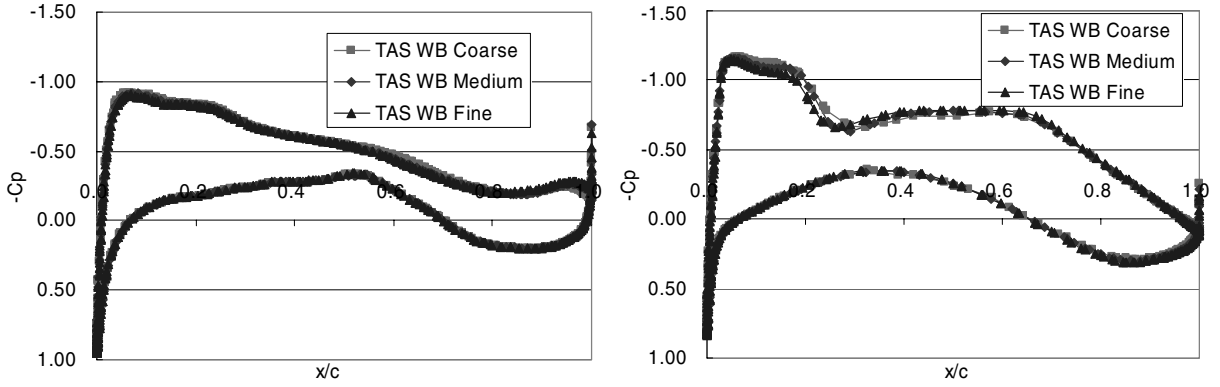

a) 15 % span location **b) 41 % span location**

Fig. 14 Comparison of the grid dependency of C_p for the WB configuration at $C_L = 0.5$; TAS original scheme, full-NS, SA.

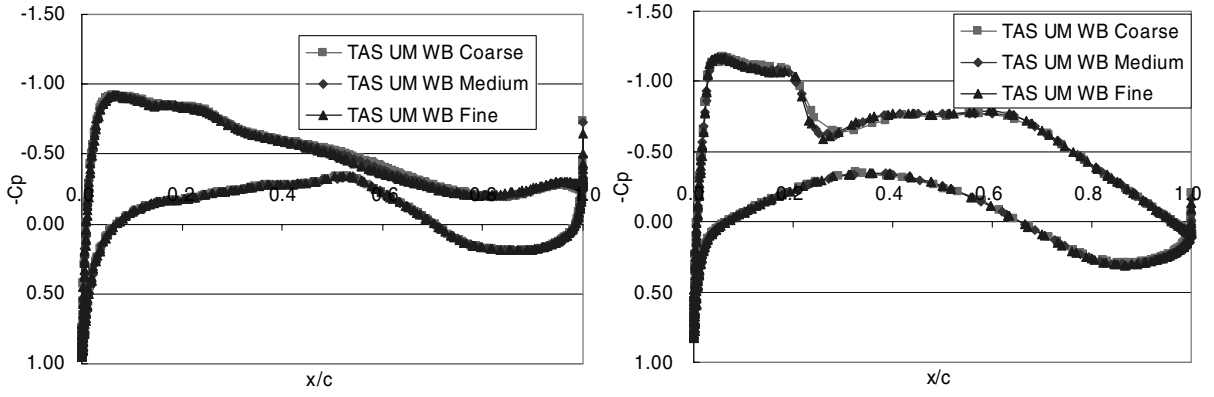

a) 15 % span location **b) 41 % span location**

Fig. 15 Comparison of the grid dependency of C_p for the WB configuration at $C_L = 0.5$; TAS U-MUSCL, full-NS, SA.

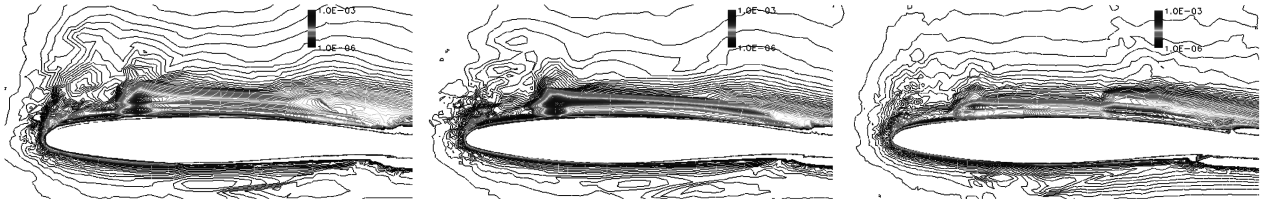

a) Coarse grid **b) Medium grid** **c) Fine grid**

Fig. 16 Contours (range from 10^{-6} to 10^{-3}) of the entropy variation change; TAS original scheme, full-NS, SA.

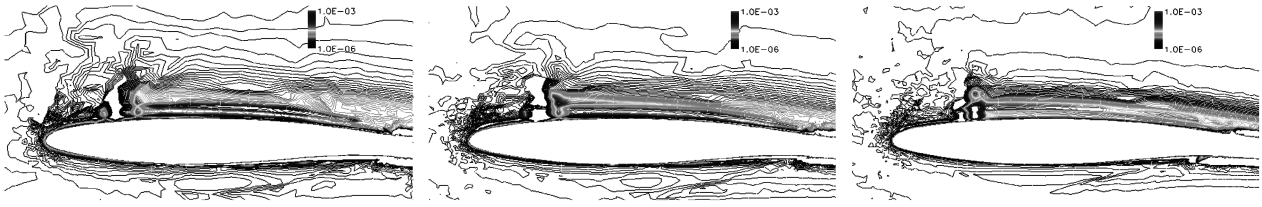

a) Coarse grid b) Medium grid c) Fine grid

Fig. 17 Contours (range from 10^{-6} to 10^{-3}) of the entropy variation change; TAS U-MUSCL, full-NS, SA.

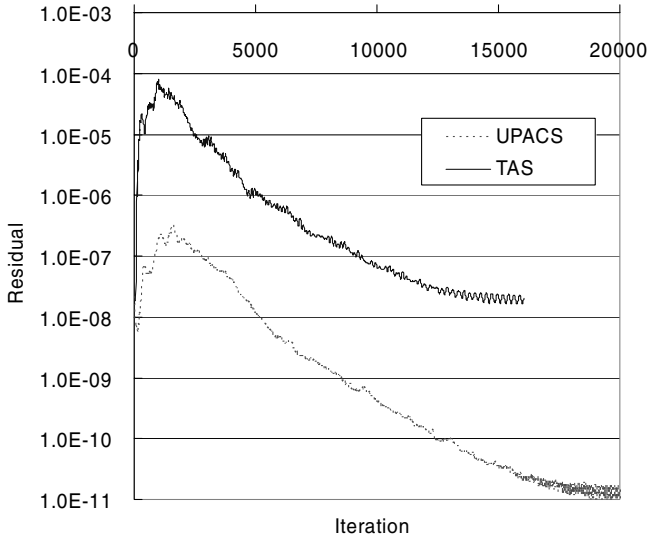

a) Residual

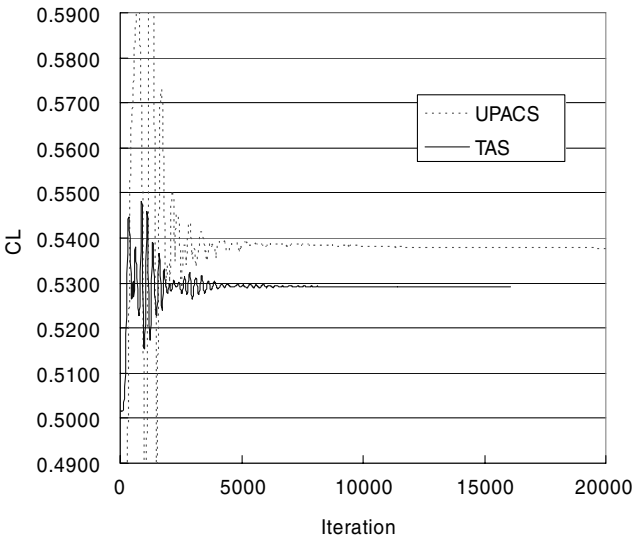

b) C_L

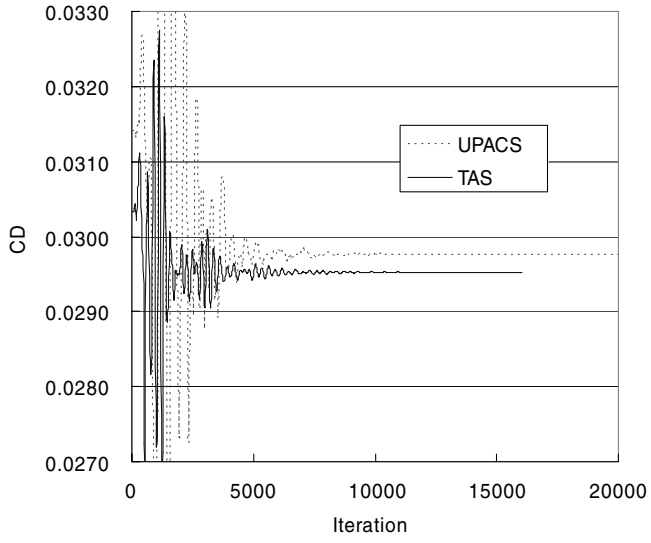

c) C_D

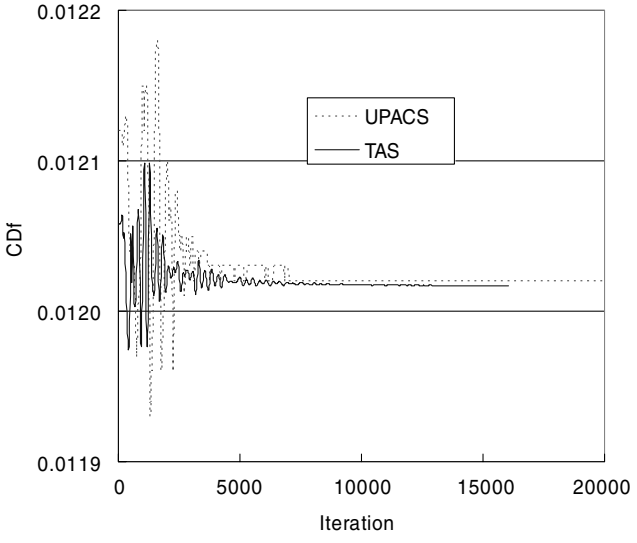

d) C_{Df}

Fig. 18 Solution convergence histories obtained on the medium grids for the WB configuration at a fixed $\alpha = 0.5$ deg by UPACS (simple-type grid, full-NS, SA) and TAS (U-MUSCL, full-NS, SA).

With the increase of α, the trailing-edge separation tends to move upstream. To investigate the effect of the grid density near the trailing edge, the results are compared on the coarse grid and the grid refined only near the trailing edge of the coarse grid using an equilateral subdivision technique [31] shown in Fig. 31. The computed forces are listed in Table 6. C_L increases by 0.004 and C_M decreases by 0.002. The increment of C_D is only 0.5 cts. Fig. 32 shows the oil-flow pattern on the refined grid at the same angle of attack. The trailing-edge separation decreases with the grid refinement.

The present unstructured grids use nearly isotropic triangles for the surface meshing, and the aspect ratio of the trailing-edge grids is nearly one. On the other hand, the present structured grids use a stretched grid in the spanwise direction. Mavriplis [32] showed that the difference of the aspect ratio in unstructured grids leads to a large change in the forces. Therefore, the effect of the spanwise grid refinement on the trailing-edge separation is investigated here by structured grids. Figure 33 shows the grids changed in the chordwise (0.5×) or spanwise resolution (4× and 8×) to the baseline coarse grid. The computational results were obtained from the restart using the result on the original coarse grid. The computed oil-flow patterns were not shown here, but all computational results did not predict the trailing-edge separation. Table 7 shows the results for drag. On the

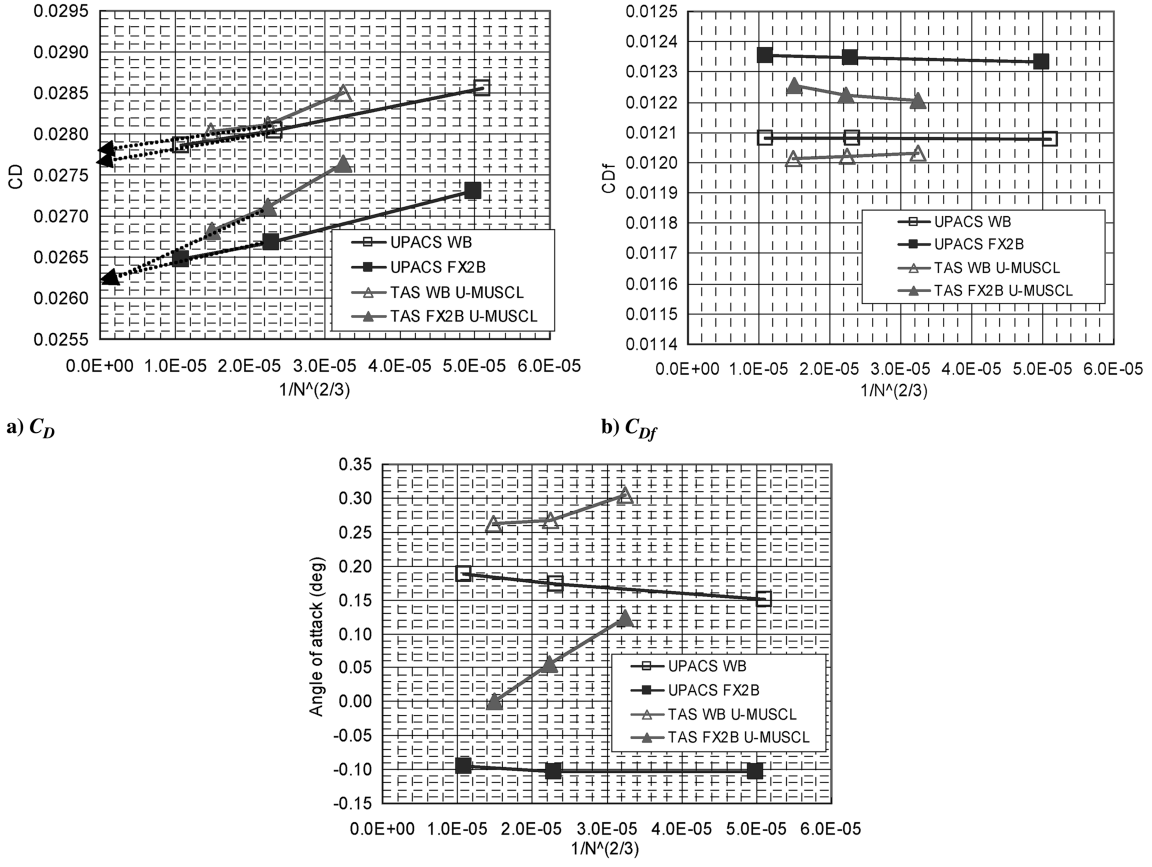

Fig. 19 Comparison of the grid convergence of C_D, C_{Df}, and angle of attack at $C_L = 0.5$ by UPACS (simple-type grid, full-NS, SA) and TAS (U-MUSCL, full-NS, SA).

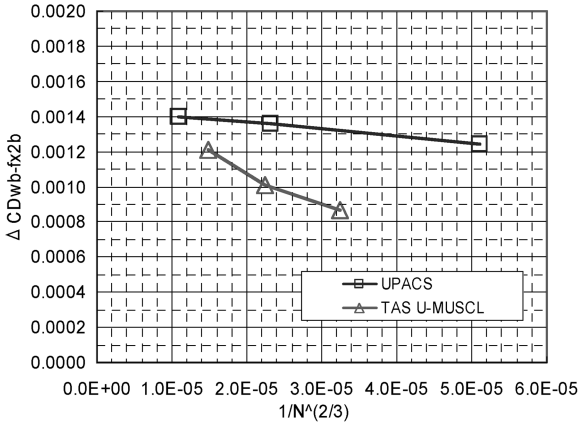

Fig. 20 Comparison of the grid convergence of $\Delta C_{D(\mathrm{WB})-(\mathrm{FX2B})}$ at $C_L = 0.5$ by UPACS (simple-type grid, full-NS, SA) and TAS (U-MUSCL, full-NS, SA).

coarser grid (0.5× in chordwise direction), the pressure drag is increased. On the other hand, the effect of the spanwise grid refinement is minimal.

C. Comparison by the Corner Grid Topology on JAXA Multiblock Structured Grids

To investigate the effect of the grid topology at the corner to the separation bubbles, the comparison of two kinds of grid topologies at the corner of the wing–body junction is performed on the JAXA multiblock structured grids. One is the simple type, in Fig. 3a, which was generated by inserting a block to keep good orthogonality at the corner. The other one is the extrude Type, in Fig. 3b, which was generated by extruding the boundary-layer grid normal to the wing and body and averaging the normal vector. The full Navier–Stokes equations are solved and the SA turbulence model is used in the comparisons.

Figure 34 shows the plots of the grid convergence of C_D, C_{Dp}, and C_{Df} at fixed $C_L = 0.5$. Regarding the FX2B configuration without the separation bubbles, the differences of C_D, C_{Dp}, and C_{Df} are minimal. Regarding the WB configuration with the separation bubbles, however, the total drag is reduced on every grid density using the extrude-type grid. Figure 35 shows the computed oil-flow patterns and C_p near the wing–body junction for the WB configuration using the extrude-type grids. Compared with the results using simple-type topology, shown in Fig. 22, the separation bubbles become smaller especially on the extrude-type coarse grid. C_{Dp} is decreased and C_{Df} is increased a little. The reduction of C_{Df} is relatively larger and it results in the reduction of the total drag. On the coarse grids, $\Delta C_{D(\mathrm{simple})-(\mathrm{extrude})}$ is about $+3.8$ drag cts. However, on the fine grids, the differences in both C_{Dp} and C_{Df} are reduced, and C_D on the infinite grid size agrees well. In the case of the WB configuration with the flow separation bubbles, the grid topology at the corner has the possibility to produce the difference of C_D by several drag counts, whereas the difference can be reduced with the grid refinement.

D. Comparison by the Turbulence Models on JAXA Multiblock Structured Grids

In this study, the SA model is used without the trip term for transition and the $ft2$ function, and with a modification of the production term as described in Sec. IV. The equations for the turbulence models are solved using the second-order scheme. First, the sensitivity study of the minor differences in the SA model is conducted on a JAXA multiblock structured grid (WB configuration, medium-size extrude-type corner grid) using UPACS. The full

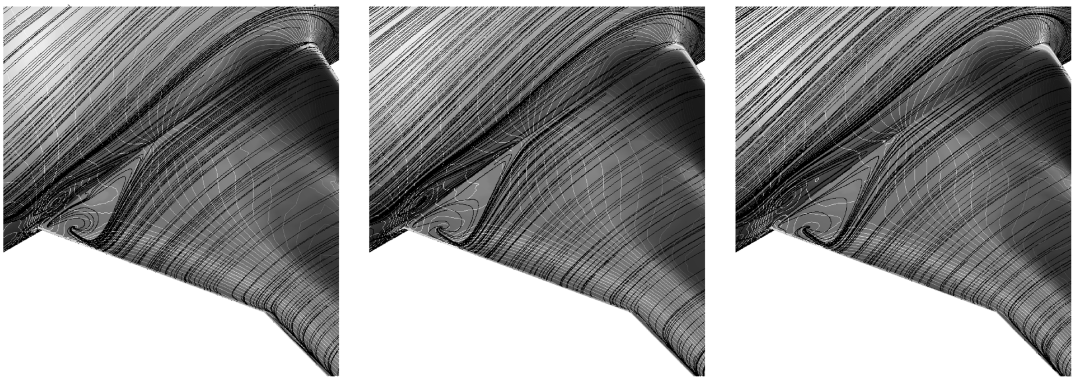

a) Coarse grid b) Medium grid c) Fine grid

Fig. 21 Comparison of C_p and oil-flow patterns near the wing–body junction for the WB configuration; TAS U-MUSCL, full-NS, SA.

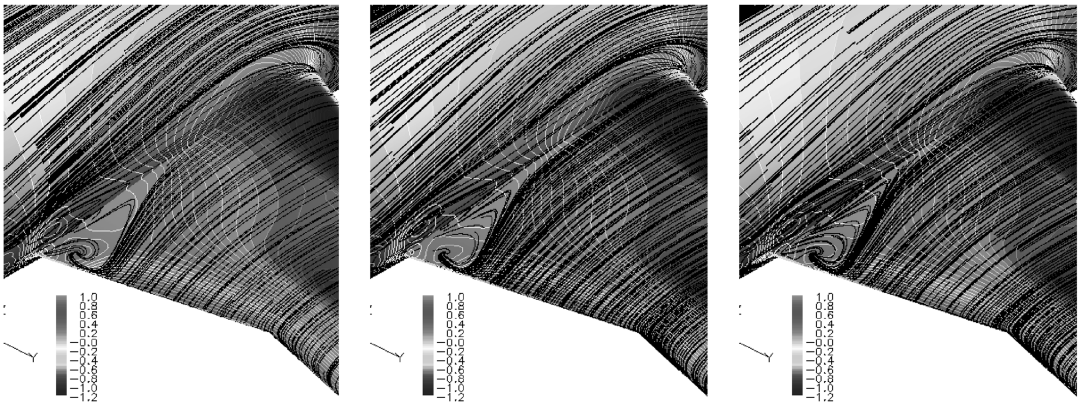

a) Coarse grid b) Medium grid c) Fine grid

Fig. 22 Comparison of C_p and oil-flow patterns near the wing–body junction for the WB configuration; UPACS simple-type grid, full-NS, SA.

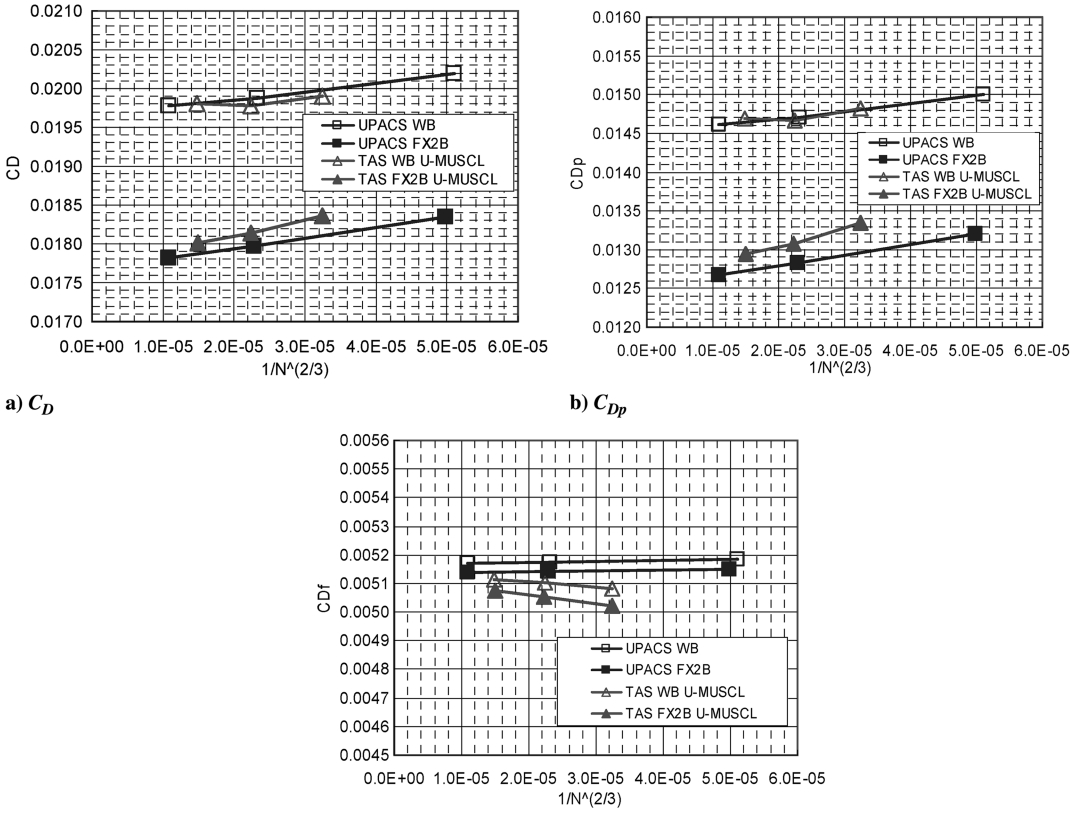

a) C_D b) C_{Dp}

c) C_{Df}

Fig. 23 Comparison of the grid convergence of C_D, C_{Dp}, and C_{Df} on the wing at $C_L = 0.5$ by UPACS (simple-type grid, full-NS, SA) and TAS (U-MUSCL, full-NS, SA).

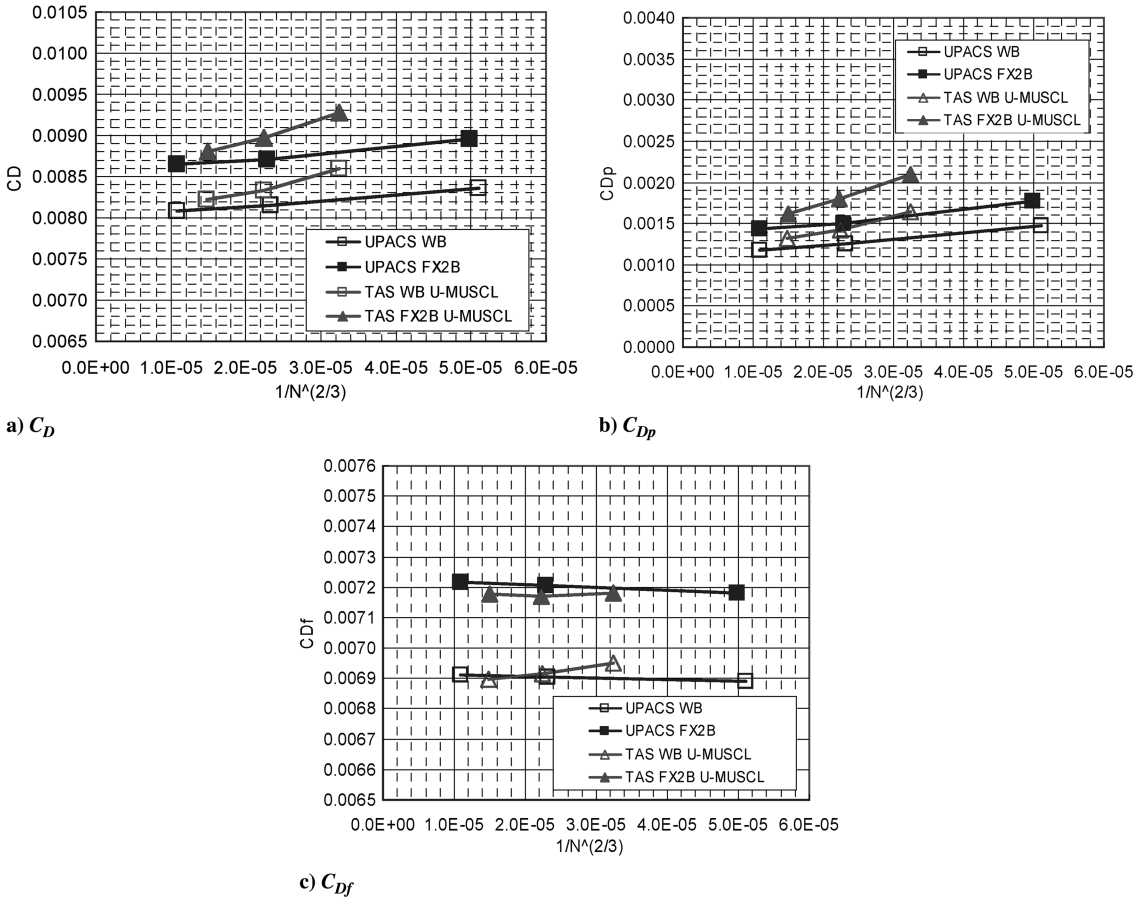

Fig. 24 Comparison of the grid convergence of C_D, C_{Dp}, and C_{Df} on the body at $C_L = 0.5$ by UPACS (simple-type grid, full-NS, SA) and TAS (U-MUSCL, full-NS, SA).

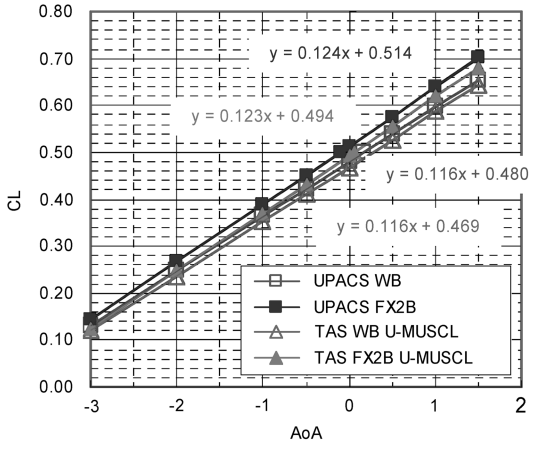

Fig. 25 Comparison of C_L-α on the medium grids by UPACS (simple-type grid, full-NS, SA) and TAS (U-MUSCL, full-NS, SA).

Navier–Stokes equations are solved in the comparisons. The effects of the $ft2$ function, the accuracy to solve the turbulence model equation, and the modification of the production term are evaluated. Table 8 summarizes the results of the sensitivity study for the drag prediction. The accuracy to solve the turbulence model equation affected the drag prediction by 1 drag cts. However, the other results showed little difference in the results even for the WB configuration with the separation bubbles.

Next, the difference by the turbulence models is evaluated on the JAXA multiblock structured grids (simple-type corner grid) using UPACS. In this study, two kinds of turbulence models explained in Sec. IV are used: the Spalart–Allmaras model [20] with a modification to reduce the eddy viscosity in the regions of high vorticity, and Menter's SST k-ω model [21]. The full Navier–Stokes equations are solved in the comparisons.

In Fig. 36, C_p distributions at 15, 41, and 84.7% span locations on the coarse grid are compared. The difference of C_p by the turbulence models is minimal, although C_p at 15% span location for the WB configuration slightly differs near the separation bubbles at the corner. Figure 37 shows the computed oil-flow patterns and C_p near the wing–body junction for the WB configuration using the SST turbulence model. Compared with the results using the SA turbulence model, shown in Fig. 22, the difference does not appear in the size of the separation bubbles but in the aspect of the center of the separation bubble. Figure 38 shows the plots of the grid convergence of C_D, C_{Dp}, and C_{Df} at fixed $C_L = 0.5$. As shown in Fig. 38c, the SST model produces lower C_{Df} for both configurations. The grid dependency is observed even for the friction drag when the SST model is used. The difference of C_{Df} between the coarse and fine grids is 3.5 cts.; $\Delta C_{Df(\mathrm{WB})-(\mathrm{FX2B})}$ is about -2.5 cts. and independent of the turbulence models and the grid size. Regarding C_{Dp}, there is a difference only for the FX2B configuration.

Figures 39 and 40 show the plots of the grid convergence of C_D, C_{Dp}, and C_{Df} on the wing and body. On the wing, the SA and SST models produce similar results. For the FX2B configuration, the gradients of the grid convergence and the drag values on the infinite grid size agree well on the wing. For both configurations, the SST model produces lower C_{Df} by about 1 cts. on the wing, whereas $\Delta C_{Df(\mathrm{WB})-(\mathrm{FX2B})}$ is consistent. The grid dependency is not observed on the wing for the friction drag even when the SST model is used. On the body, the grid dependency is observed for the friction drag when the SST model is used. However, $\Delta C_{Df(\mathrm{WB})-(\mathrm{FX2B})}$ on the body is identical for both turbulence models and every grid size. For the FX2B configuration, $\Delta C_{f(\mathrm{SST})-(\mathrm{SA})}$ on the surface of the medium grid is visualized in Fig. 41. The difference on the wing exists in the regions near the leading edge and shock wave. A large difference on

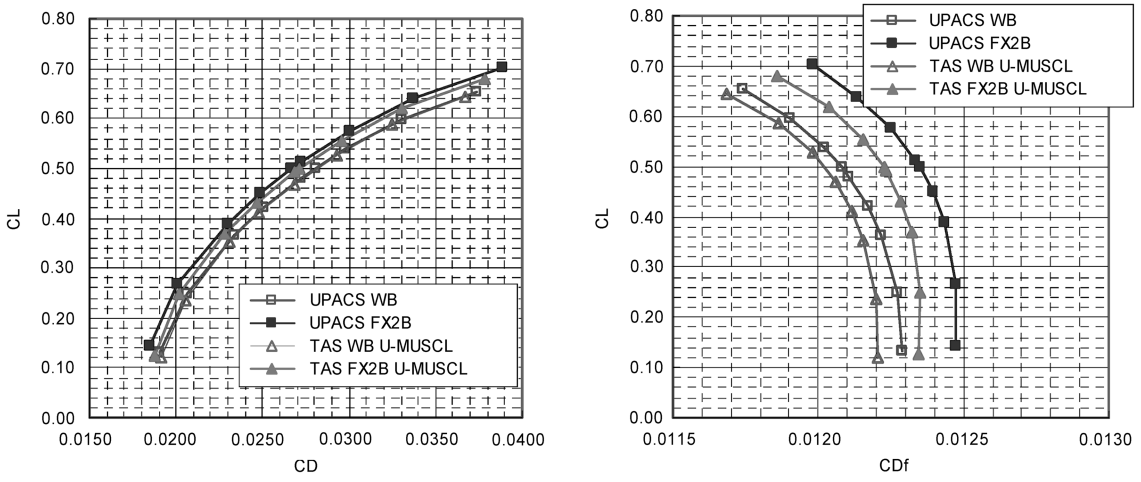

a) C_L-C_D b) C_L-C_{Df}

Fig. 26 Comparison of C_L-C_D and C_L-C_{Df} on the medium grids by UPACS (simple-type grid, full-NS, SA) and TAS (U-MUSCL, full-NS, SA).

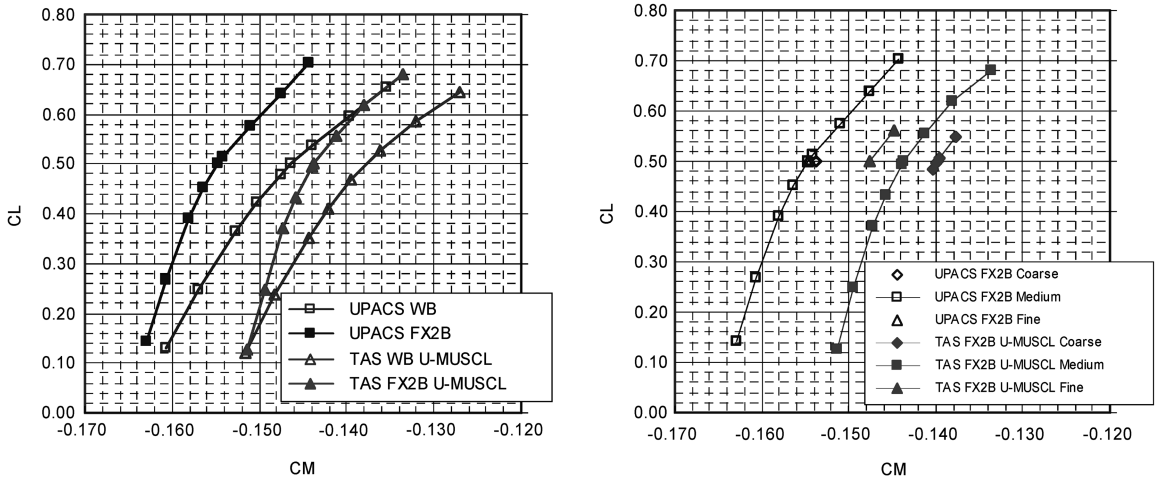

a) C_L-C_M on the medium grids b) Grid dependency of C_L-C_M for the FX2B configuration

Fig. 27 Comparison of C_L-C_M by UPACS (simple-type grid, full-NS, SA) and TAS (U-MUSCL, full-NS, SA).

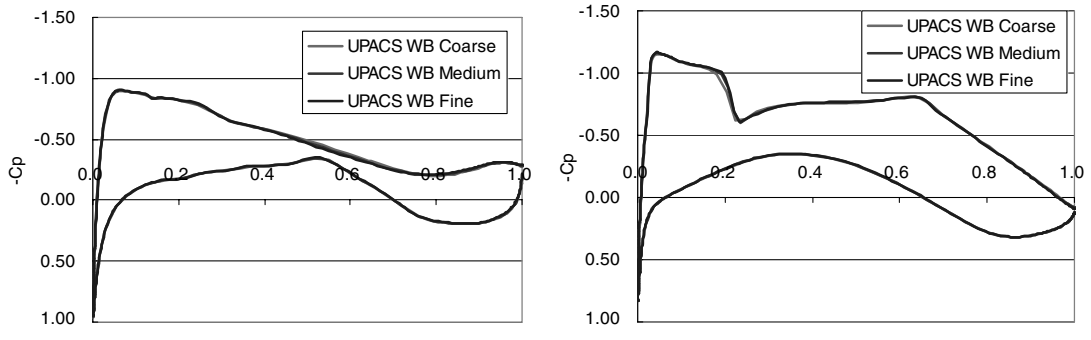

a) 15% span location b) 41% span location

Fig. 28 Comparison of the grid dependency of C_p for the WB configuration at $C_L = 0.5$; UPACS simple-type grid, full-NS, SA.

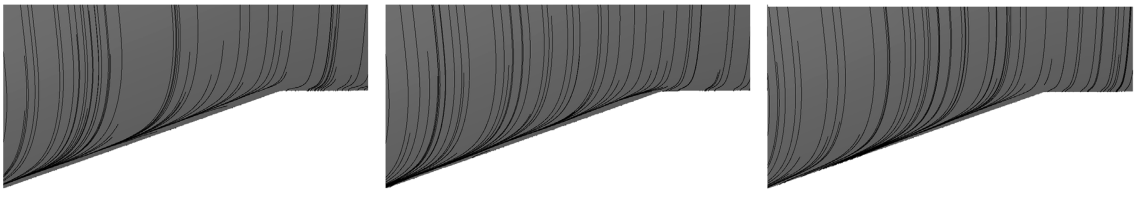

a) Coarse grid (α=0.123°) b) Medium grid (α=0.056°) c) Fine grid (α=0.0°)

Fig. 29 Comparison of the oil-flow patterns near the kink trailing edge at $C_L = 0.5$ for the FX2B configuration; TAS U-MUSCL, full-NS, SA.

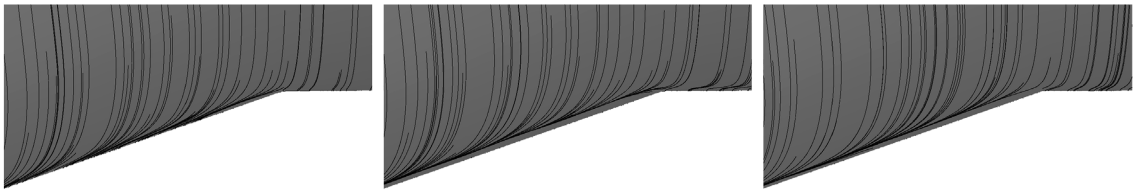

a) Medium grid at α=-0.5° b) Medium grid at α=0.5° c) Fine grid at α=0.5°

Fig. 30 Comparison of the oil-flow patterns near the kink trailing edge for the FX2B configuration at different α; TAS U-MUSCL, full-NS, SA.

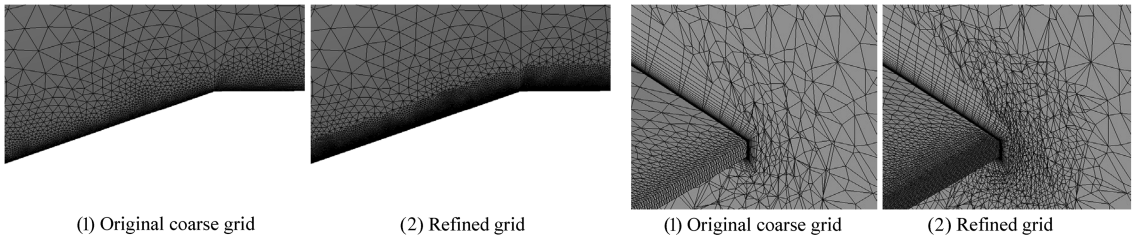

a) Surface grid near the kink trailing-edge b) Cross-sectional views of the grid at the kink

Fig. 31 Comparison of the coarse grid and the grid refined only near the trailing edge of the coarse grid using a subdivision technique.

the body exists in the region near the leading edge at the wing–body junction. The three-dimensional flow at the corner near the leading edge has the possibility to generate a difference on the body. More detailed and additional validation studies have to be conducted on the three-dimensional flow at the corner for the turbulence models.

E. Comparison by the Thin-Layer Approximation on JAXA Multiblock Structured Grids

To investigate the effect of the thin-layer approximation for viscous terms, the results by solving the full Navier–Stokes equations and thin-layer Navier–Stokes equations are compared on the JAXA multiblock structured grids. Both simple-type and extrude-type corner grids are used to evaluate. The SA turbulence model is used.

Figure 42 shows the plots of the grid convergence of C_D, C_{Dp}, and C_{Df} at fixed $C_L = 0.5$. Angles of attack to keep $C_L = 0.5$ are also plotted in Fig. 42d. For the FX2B configuration, the thin-layer results produce lower C_{Dp} by 1 drag cts. on every grid including simple type and extrude type, as shown in Fig. 42b. For the WB configuration with the separation bubbles, the difference by the thin-layer approximation is significantly larger. The thin-layer results for the WB configuration produce lower C_D by 9 drag cts. on simple-type grids and $9 \sim 13$ drag cts. on extrude-type grids. Figures 43 and 44 show the computed oil-flow patterns and C_p near the wing–body junction for the WB configuration solving the thin-layer Navier–Stokes equations on simple-type and extrude-type corner grids. Comparison of the results with/without the thin-layer approximation on simple-type grids in Figs. 21 and 43 shows the separation bubbles become smaller on every grid density. C_{Dp} is decreased by 9 drag cts. and C_{Df} is increased a little. Comparison of the results on extrude-type grids in Figs. 35 and 44 shows the separation bubbles become extremely smaller on every grid density. C_{Dp} is largely reduced to the level of the FX2B configuration and the total C_D becomes nearly identical with that of the FX2B configuration. As shown in Fig. 42d, the angles of attack to keep $C_L = 0.5$ are decreased due to the decrease of the separation bubbles and it may also lead to the reduction.

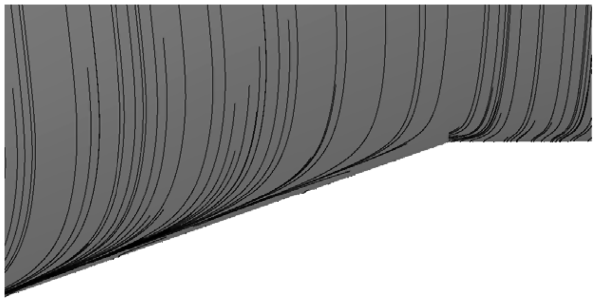

Fig. 32 Oil-flow pattern near the kink trailing edge on the trailing-edge refined grid at $\alpha = 0.123$ deg for the FX2B configuration; TAS U-MUSCL, full-NS, SA.

The thin-layer approximation omits the cross terms at the evaluation of the velocity gradient for the viscous flux for Navier–Stokes equations and the eddy viscosity gradient for the diffusion term for the turbulence model. Then, it should cause a strong grid dependency in the diffusion on the cross-section at the corner flow separation, especially when skewed grids like the extrude type are used.

F. Comparison by JAXA and Boeing Multiblock Structured Grids

The results using the Boeing multiblock structured grid that is available on the DPW-3 Web site[‡] are compared. The computations using the Boeing grid were conducted only on the medium size grid for the DLR-F6 WB configuration. The Boeing grids use the extrude-type grid at the corner of the wing–body junction. The results solving the full Navier–Stokes equations and thin-layer Navier–Stokes equations are compared. The SA turbulence model is used.

Figure 45 shows the computed oil-flow patterns and C_p near the wing–body junction for the WB configuration without and with the thin-layer approximation on the Boeing medium grid. The size of the

Table 6 Aerodynamic forces with and without grid refinement near the wing trailing edge on unstructured grids

Grid	α	C_L	C_D	C_{Dp}	C_{Df}	C_M
Coarse grid	0.1228	0.5000	276.3×10^{-4}	154.3×10^{-4}	122.0×10^{-4}	−0.1398
Refined grid	0.1228	0.5046	276.8×10^{-4}	154.8×10^{-4}	122.0×10^{-4}	−0.1417

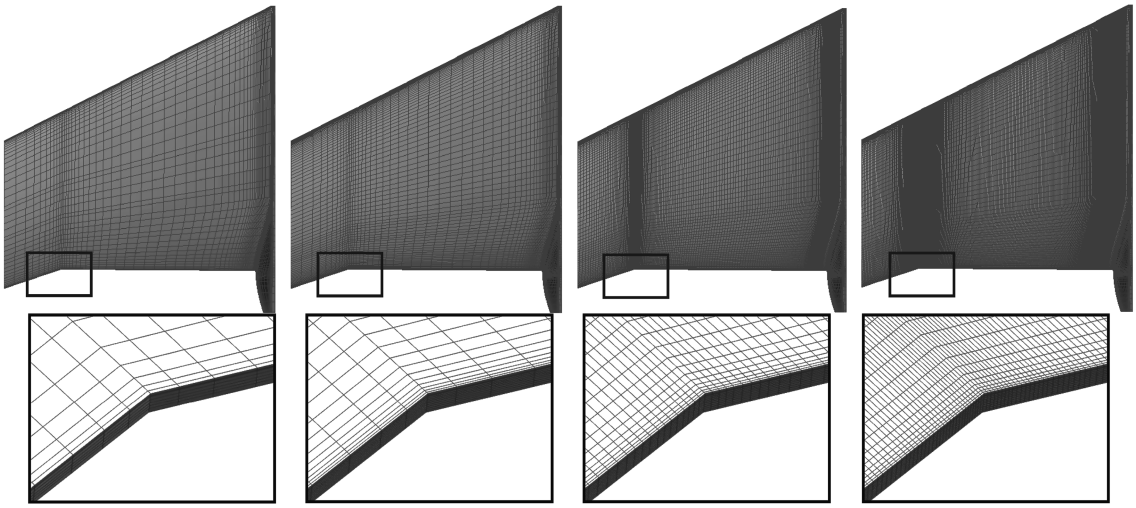

a) 0.5× chordwise resolution b) Baseline coarse grid c) 4× spanwise resolution d) 8× spanwise resolution

Fig. 33 Structured grids changed in the chordwise or spanwise resolution to the baseline coarse grid.

separation bubbles without the thin-layer approximation is similar to the results on the JAXA grids. The separation bubbles become smaller with the thin-layer approximation, which is also the same tendency with the results on the JAXA grids. C_D, C_{Dp}, and C_{Df} at fixed $C_L = 0.5$ on the medium grid for the WB configuration are plotted in Fig. 46. The results on both simple-type and extrude-type JAXA multiblock structured grids are also plotted in the figures. Comparison of the results with/without the thin-layer approximation shown in Fig. 46 shows that C_D with the thin-layer approximation is reduced due to the decrease of the separation bubbles. The tendency of the results on the Boeing grid is consistent with the results on the JAXA grids. The absolute values of C_D on the Boeing medium grid are also similar with the results on the JAXA extrude-type medium grid, although the Boeing medium grid produces slightly lower C_D by $1 \sim 2$ cts. due to the difference in C_{Df} by 1 cts.

VII. Conclusions

Comparison studies of computations for DPW-3 have been performed on the DLR-F6 wing–body configurations with and without the wing–body fairing using the structured grid solver UPACS and unstructured grid solver TAS code. The self-made multiblock structured grids and mixed-element unstructured grids were employed. The medium size grid of the Boeing multiblock structured grids, which were available on the DPW-3 Web site, was also compared.

The comparisons between the two codes have been conducted using the same SA turbulence model. The reconstruction schemes to realize the second-order spatial accuracy have been also compared on unstructured grids and the results showed that the U-MUSCL scheme reduced the numerical dissipation and largely improved the grid convergence of the drag. The comparisons between the two codes showed that both results by UPACS and TAS were consistent for the grid convergence of drag, the size of the flow separation, the incremental drag between configurations, and α sweep on the medium grids when the same turbulence model was used. The gradients of the grid convergence were different, whereas the values on the infinite grid size were nearly the same for both configurations. The relatively larger grid dependency of C_D on the unstructured grids came from the difference of C_{Dp} on the body and from the insufficient grid resolution of the body on the coarse and medium grids. More careful and experienced gridding guidelines will be required on the body for our unstructured grids.

In addition, detailed comparisons have been conducted on the grid topology at the corner of the wing–body junction, the turbulence models, and the thin-layer approximation in viscous terms, using the multiblock structured grids to clarify the sensitivity of drag prediction to these factors.

The comparisons of the grid topology at the corner showed that, in the case with the flow separation bubbles, the extrude-type corner grid topology produced lower C_D by several drag counts due to the decrease of the flow separation bubbles than the simple-type corner grid, whereas the difference is reduced with the grid refinement.

The comparisons of the SA and SST turbulence models showed that the SST model produced lower C_{Df} for both configurations, whereas ΔC_D between the configurations was nearly identical. The difference tended to be reduced with the grid refinement. The difference of the flow separation bubbles did not appear in the size but in the aspect of the center of the separation bubble. The grid dependency of C_{Df} by the SST model came from the body, and large difference in $\Delta C_{f(\mathrm{SST})-(\mathrm{SA})}$ existed in the region near the leading edge at the wing–body junction. A more detailed validation study has to be conducted on the three-dimensional flow at the corner near the leading edge.

The comparisons with/without the thin-layer approximation showed that the thin-layer approximation reduced the size of the separation bubbles and resulted in lower C_D by $9 \sim 13$ drag cts. for the WB configuration. The approximation caused a strong grid dependency at the corner flow separation, especially when skewed grids like the extrude type were used. The results using the medium size grid of the Boeing grids also showed the same tendency with the results on the JAXA grids.

In the present computations for the WB configuration excluding the thin-layer approximation, the variations of C_D by the numerical methods including the grids and turbulence models were about 10 cts. ($3 \sim 4\%$) on the coarse grids ($3 \sim 5$ million grid points) and about 4 cts. ($1 \sim 2\%$) on the fine grids ($17 \sim 29$ million grid points). The variation by the numerical methods decreases with the grid size.

Table 7 Comparions of C_{Dp} and C_{Df} on the structured grids changed in the spanwise resolution

Grid	0.5× chordwise	Baseline coarse grid	4× spanwise	8× spanwise
C_{Dp}	161×10^{-4}	150×10^{-4}	149×10^{-4}	149×10^{-4}
C_{Df}	123×10^{-4}	123×10^{-4}	123×10^{-4}	123×10^{-4}

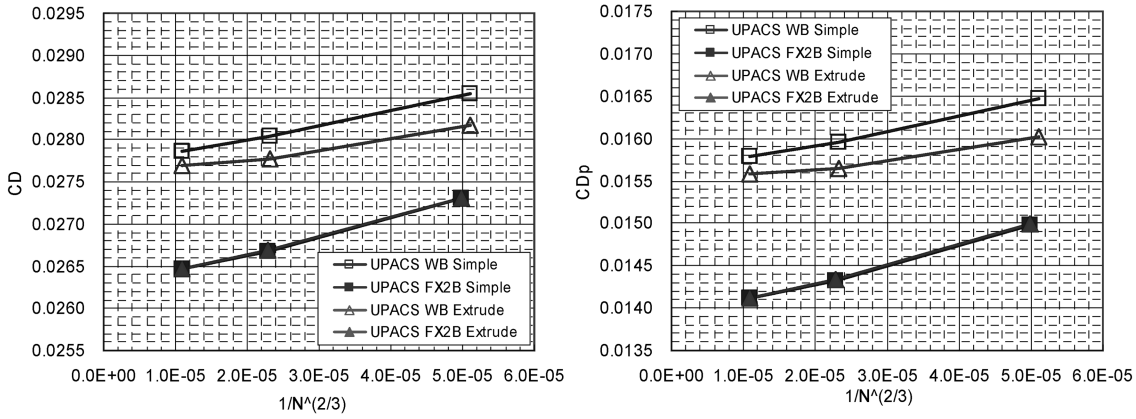

a) C_D b) C_{Dp}

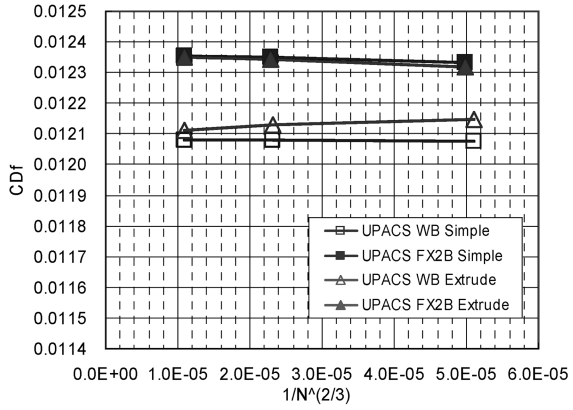

c) C_{Df}

Fig. 34 Comparison of the grid convergence of C_D, C_{Dp}, and C_{Df} at $C_L = 0.5$ by the grid topology at the corner of the wing–body junction; UPACS, full-NS, SA.

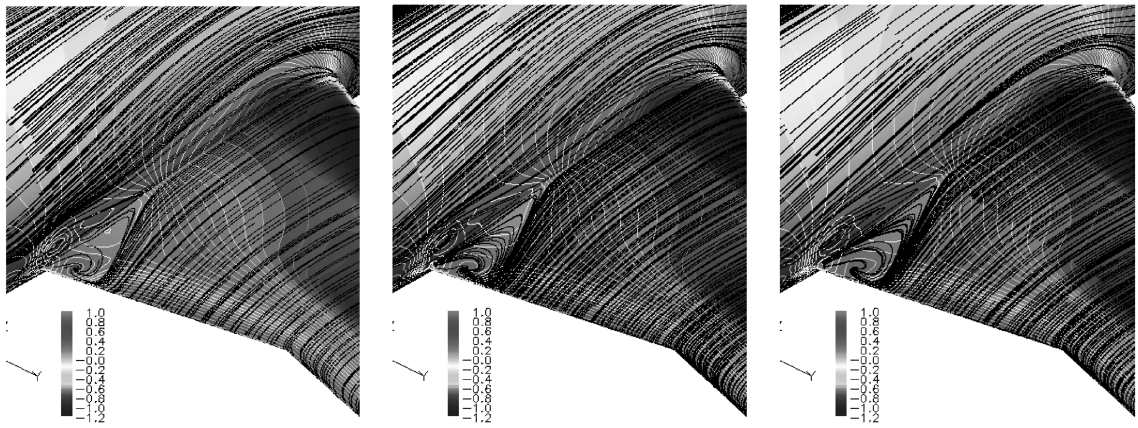

a) Coarse grid b) Medium grid c) Fine grid

Fig. 35 Comparison of C_p and the oil-flow patterns near the wing–body junction for the WB configuration; UPACS extrude-type grid, full-NS, SA.

Table 8 Sensitivity study of the minor differences in the Spalart–Allmaras turbulence model

SA model	Ft2 function	Accuracy to solve turbulent model Eqs.	S in production term	Angle of attack	C_L	C_{Dp}	C_{Df}	C_D
Present SA model	without	second-order	min (vorticity, strain rate)	0.1272	0.50004	0.01565	0.01213	0.02778
Model A	with	second-order	min (vorticity, strain rate)	0.1272	0.49996	0.01565	0.01213	0.02778
Model B	without	first-order	min (vorticity, strain rate)	0.1160	0.50001	0.01552	0.01213	0.02765
Model C	without	second-order	vorticity	0.1000	0.50014	0.01558	0.01218	0.02776

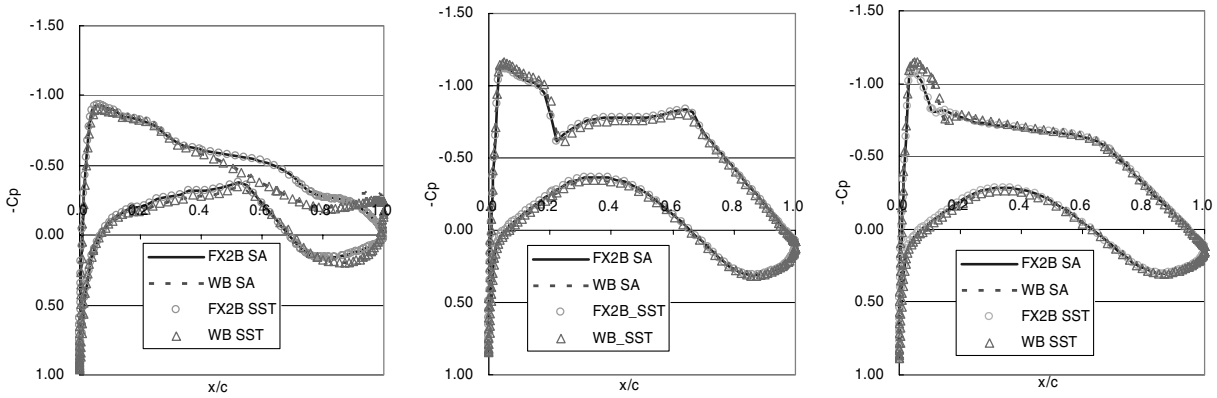

a) 15% span location b) 41% span location c) 84.7% span location

Fig. 36 Comparison of C_p on the coarse grid by the turbulence models for the FX2B and WB configurations at $C_L = 0.5$; UPACS simple-type grid, full-NS.

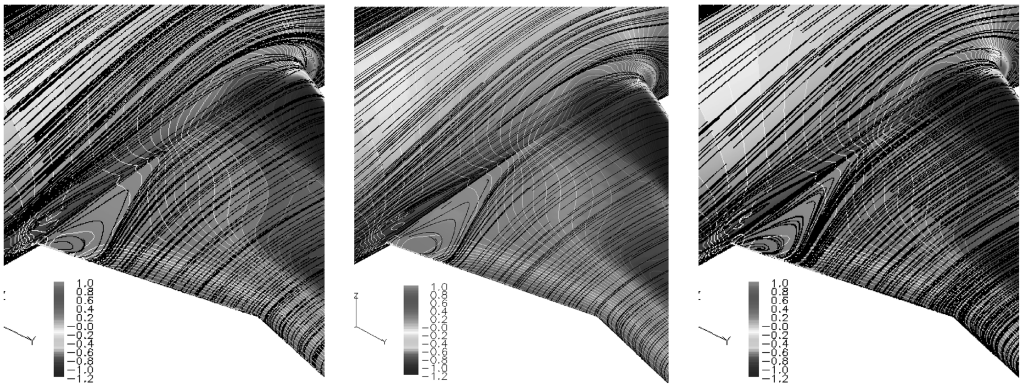

a) Coarse grid b) Medium grid c) Fine grid

Fig. 37 Comparison of C_p and the oil-flow patterns near the wing–body junction for the WB configuration; UPACS simple-type grid, full-NS, SST.

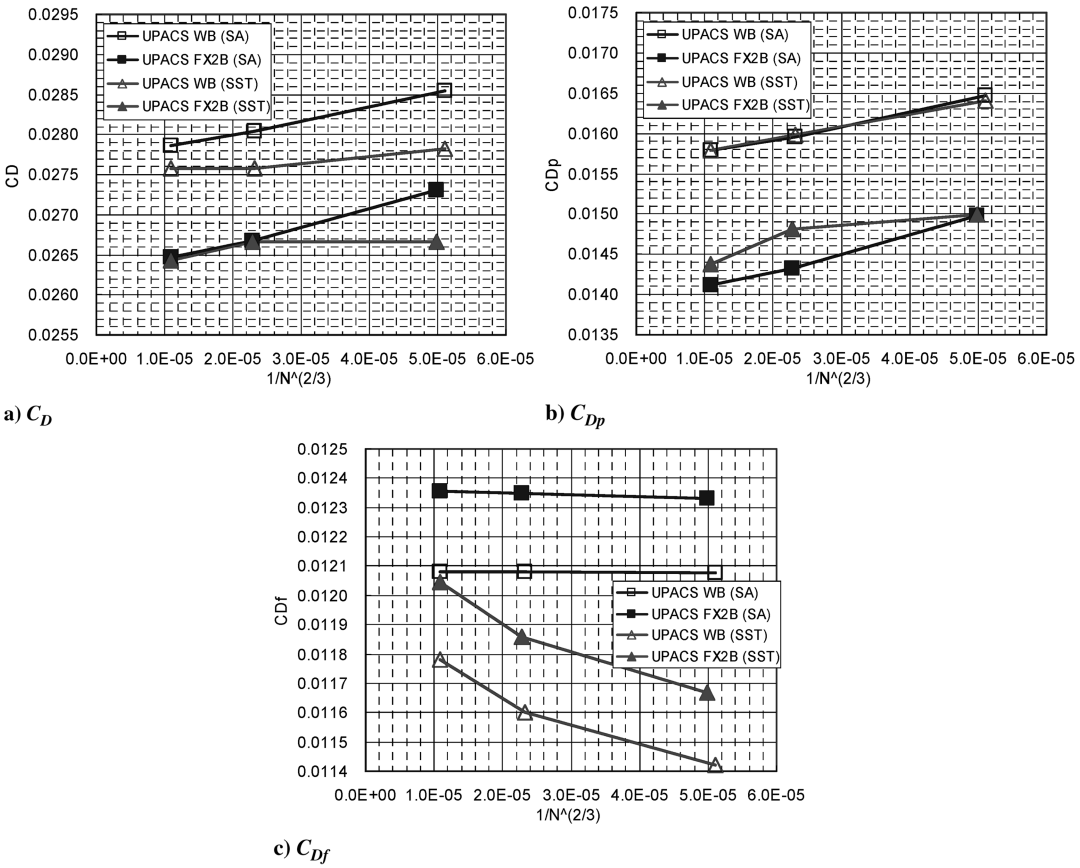

a) C_D b) C_{Dp}

c) C_{Df}

Fig. 38 Comparison of the grid convergence of C_D, C_{Dp}, and C_{Df} at $C_L = 0.5$ by the turbulence models; UPACS simple-type grid, full-NS.

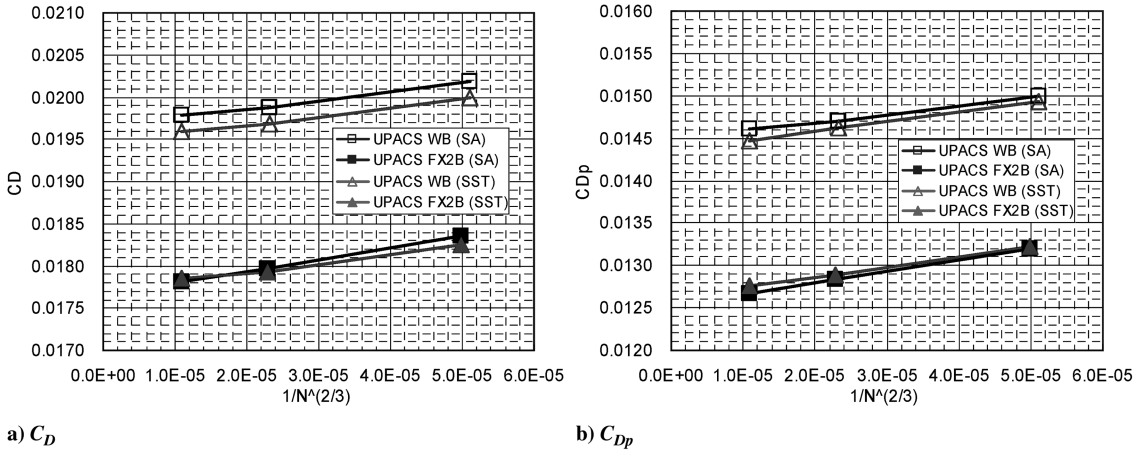

a) C_D b) C_{Dp}

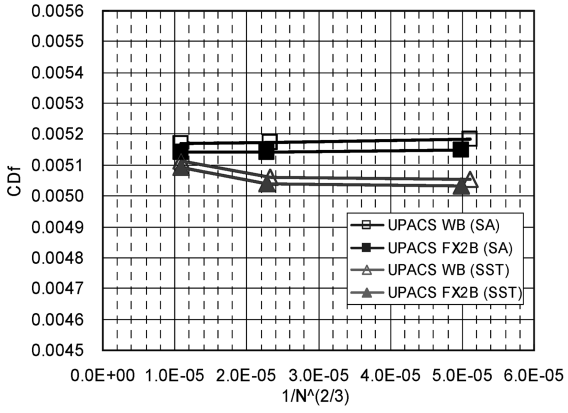

c) C_{Df}

Fig. 39 Comparison of the grid convergence of C_D, C_{Dp}, and C_{Df} on the wing at $C_L = 0.5$ by the turbulence models; UPACS simple-type grid, full-NS.

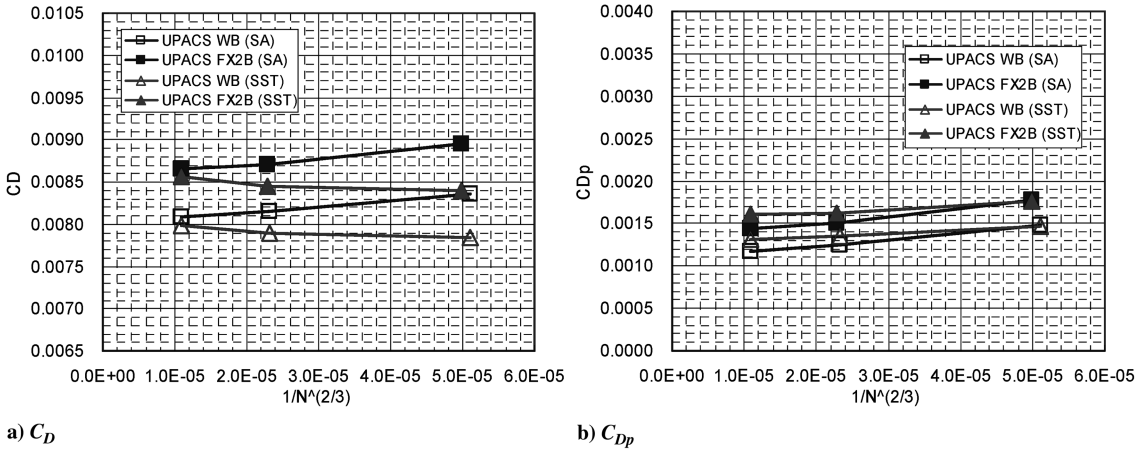

a) C_D b) C_{Dp}

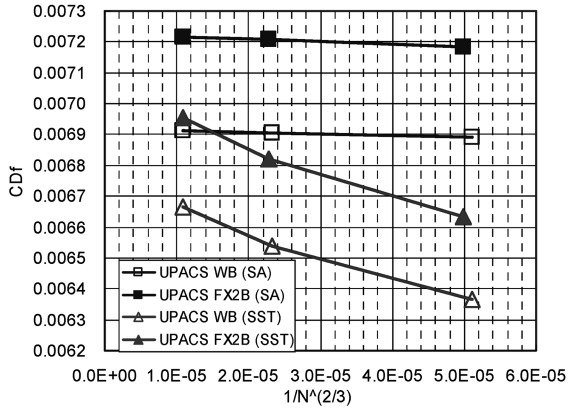

c) C_{Df}

Fig. 40 Comparison of the grid convergence of C_D, C_{Dp}, and C_{Df} on the body at $C_L = 0.5$ by the turbulence models; UPACS simple-type grid, full-NS.

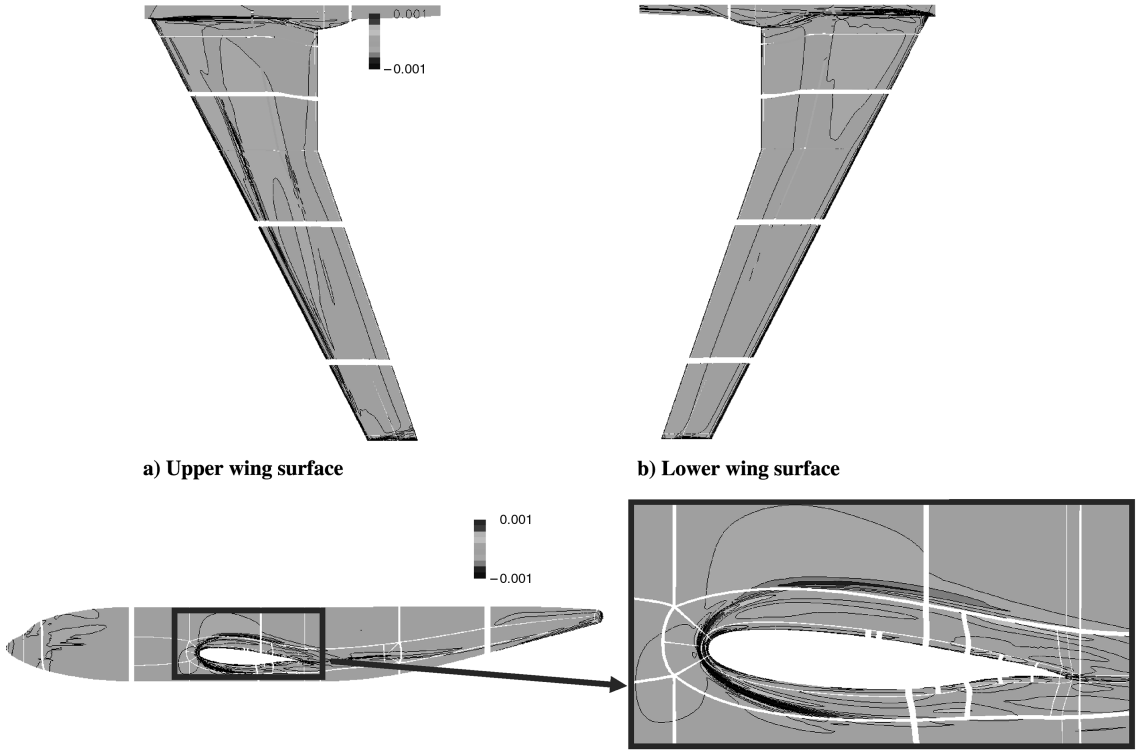

Fig. 41 $\Delta C_{f(\mathrm{SST})-(\mathrm{SA})}$ **on the surface of the medium grid for the FX2B configuration at** $C_L = 0.5$**; UPACS simple-type grid, full-NS.**

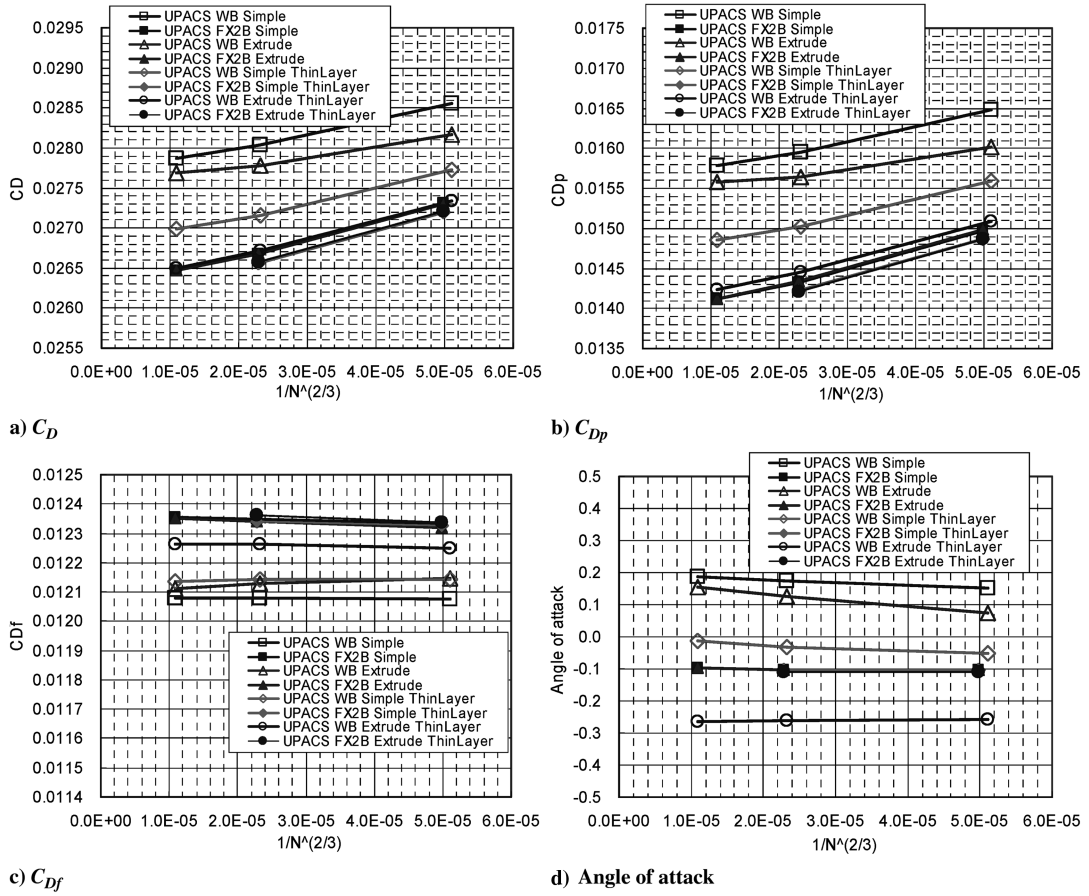

Fig. 42 Comparison of the grid convergence of C_D**,** C_{Dp}**,** C_{Df}**, and angle of attack at** $C_L = 0.5$ **by the approximation for viscous terms; UPACS simple-type grid, SA.**

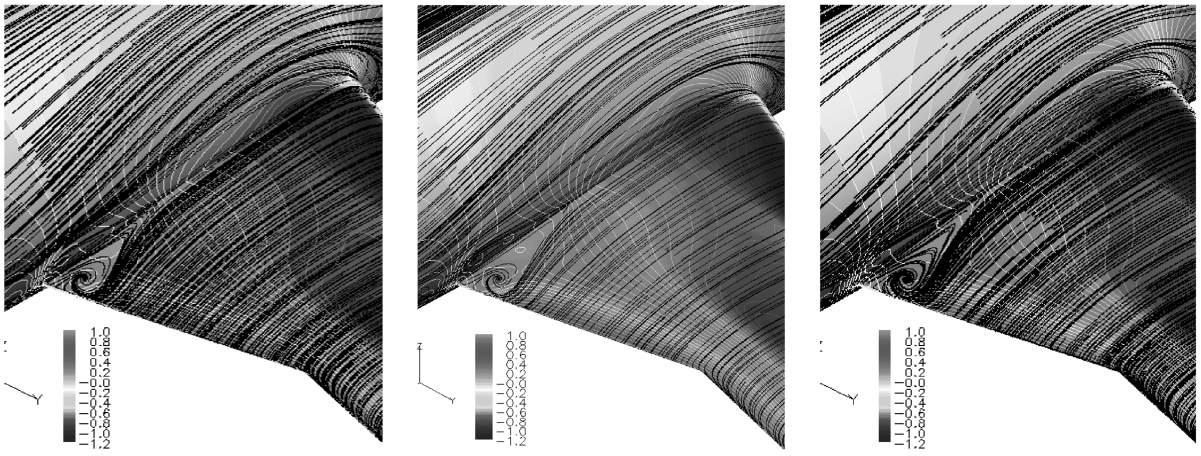

a) Coarse grid b) Medium grid c) Fine grid

Fig. 43 Comparison of C_p and the oil-flow patterns near the wing–body junction for the WB configuration; UPACS simple-type grid, thin-layer NS, SA.

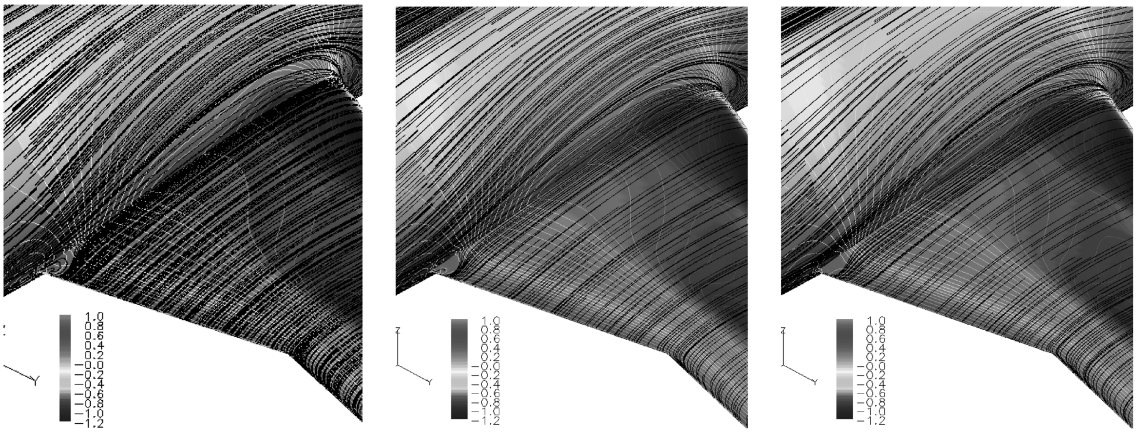

a) Coarse grid b) Medium grid c) Fine grid

Fig. 44 Comparison of C_p and the oil-flow patterns near the wing–body junction for the WB configuration; UPACS extrude-type grid, thin-layer NS, SA.

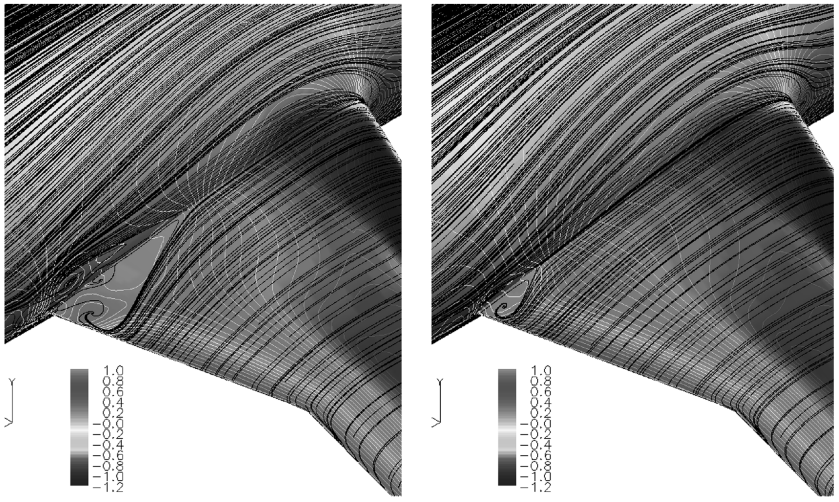

a) Without thin-layer approximation b) With thin-layer approximation

Fig. 45 Comparison of C_p and the oil-flow patterns near the wing–body junction for the WB configuration on the Boeing medium grid; UPACS, SA.

Regarding the FX2B configuration without the flow separation bubbles, the variations by the numerical methods were much smaller and all results were almost identical. Through this study, the grid dependency has been clarified. However, the quantitative prediction to the configuration with the flow separation bubbles still has difficulty. Study of the turbulence models for the corner flow separation is the next step. In this study, practical and widely used turbulence models have been evaluated. The applicability and characteristics related to the grid for the corner flow separation should be investigated further in conjunction with the wind-tunnel

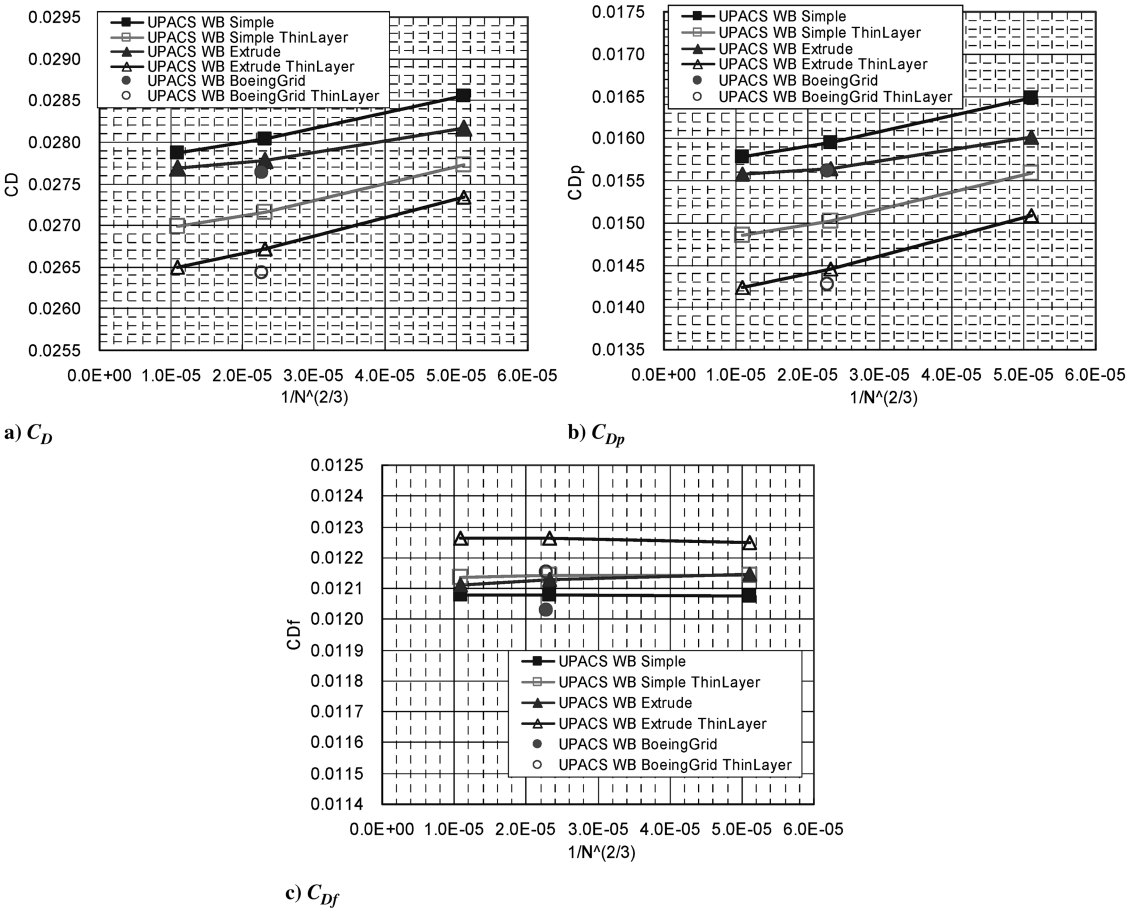

Fig. 46 Comparison of the grid convergence of C_D, C_{Dp}, C_{Df} at $C_L = 0.5$ by the JAXA and Boeing grids and the approximation for viscous terms; UPACS, SA.

tests. In addition, the turbulence models considering the physics of the flows at the corner also should be studied.

Acknowledgments

The authors would like to thank Tohru Hirai and Kentaro Tanaka of Ryoyu Systems Company, Ltd., Ryozo Ito of Daiko Denshi Tsushin, Ltd., Hiroaki Ishikawa of Sanko Software Development Company, Ltd., and Zhong Lei of Aviation Program Group in Japan Aerospace Exploration Agency for their contributions and useful discussions.

References

[1] Levy, D. W., Zickuhr, T., Vassberg, J., Agrawal, S., Wahls, R. A., Pirzadeh, S., and Hemsch, M. J., "Data Summary from the First AIAA Computational Fluid Dynamics Drag Prediction Workshop," *Journal of Aircraft*, Vol. 40, No. 5, 2003, pp. 875–882.

[2] Hemsh, M. J., "Statistical Analysis of Computational Fluid Dynamics Solutions from the Drag Prediction Workshop," *Journal of Aircraft*, Vol. 41, No. 1, 2004, pp. 95–103.

[3] Laflin, K. R., Klausmeyer, S. M., Zickuhr, T., Vassberg, J. C., Wahls, R. A., Morrison, J. H., Brodersen, O. P., Rakowitz, M. E., Tinoco, E. N., and Godard, J-L., "Data Summary from Second AIAA Computational Fluid Dynamics Drag Prediction Workshop," *Journal of Aircraft*, Vol. 42, No. 5, 2005, pp. 1165–1178.

[4] Hemsch, M. J., and Morrison, J. H., "Statistical Analysis of CFD Solutions from 2nd Drag Prediction Workshop," AIAA Paper 2004-0556, Jan. 2004.

[5] Vassberg, J. C., Tinoco, E. N., Mani, M., Brodersen, O. P., Eisfeld, B., Wahls, R. A., Morrison, J. H., Zickuhr, T., Laflin, K. R., and Mavriplis, D. J., "Summary of the Third AIAA CFD Drag Prediction Workshop," AIAA Paper 2007-0260, Jan. 2007.

[6] Morrison, J. H., and Hemsch, M. J., "Statistical Analysis of CFD Solutions from the Third AIAA Drag Prediction Workshop," AIAA Paper 2007-0254, Jan. 2007.

[7] Vassberg, A., Sclafani, A., and DeHaan, M., "Wing-Body Fairing Design for the DLR-F6 Model: A DPW-III Case Study," AIAA Paper 2005-4730, June 2005.

[8] Yamamoto, K., Ochi, A., Shima, E., and Takaki, R., "CFD Sensitivity of Drag Prediction on DLR-F6 Configuration by Structured Method and Unstructured Method," AIAA Paper 2004-0398, Jan. 2004.

[9] Brodersen, O., and Stuermer, A., "Drag Prediction of Engine-Airframe Interference Effects Using Unstructured Navier–Stokes Calculations," AIAA Paper 2001-2414, June 2001.

[10] Takaki, R., Yamamoto, K., Yamane, T., Enomoto, S., and Mukai, J., "Development of the UPACS CFD Environment," *High Performance Computing, Proceedings of the 5th International Symposium of ISHPC 2003*, edited by Vie-denbaum, Joe, K., Amano, H., and Aiso, H., Springer–Verlag, Berlin, 2003, pp. 307–319.

[11] Imamura, T., Enomoto, S., Yokokawa, Y., and Yamamoto, K., "Simulation of the Broadband Noise from a Slat Using Zonal LES/RANS Hybrid Method," AIAA Paper 2007-0226, Jan. 2007.

[12] Roe, P. L., "Approximate Riemann Solvers, Parameter Vectors, and Difference Schemes," *Journal of Computational Physics*, Vol. 43, No. 2, 1981, pp. 57–372.

[13] van Albada, G. D., van Leer, B., and Roberts, W. W., Jr., "Comparative Study of Computational Methods in Cosmic Gas Dynamics," *Astronomy and Astrophysics*, Vol. 108, No. 1, April 1982, pp. 76–84.

[14] Shima, E., "Simple Implicit Scheme for Structured/Unstructured CFD," *Proceedings of 29th Fluid Dynamics Symposium*, 1997, pp. 325–328 (in Japanese).

[15] Nakahashi, K., Ito, Y., and Togashi, F., "Some Challenges of Realistic Flow Simulations by Unstructured Grid CFD," *International Journal for Numerical Methods in Fluids*, Vol. 43, Nos. 6–7, Oct. 2003, pp. 769–783.
doi:10.1002/fld.559

[16] Obayashi, S., and Guruswamy, G. P., "Convergence Acceleration of an Aeroelastic Navier–Stokes Solver," *AIAA Journal*, Vol. 33, No. 6, 1995, pp. 1134–1141.

[17] Sharov, D., and Nakahashi, K., "Reordering of Hybrid Unstructured Grids for Lower-Upper Symmetric Gauss–Seidel Computations," *AIAA Journal*, Vol. 36, No. 3, 1998, pp. 484–486.

[18] Venkatakrishnan, V., "Convergence to Steady State Solutions of the Euler Equations on Unstructured Grids with Limiters," *Journal of Computational Physics*, Vol. 118, No. 1, April 1995, pp. 120–130. doi:10.1006/jcph.1995.1084

[19] Burg, C., "Higher Order Variable Extrapolation for Unstructured Finite Volume RANS Flow Solvers," AIAA Paper 2005-4999, June 2005.

[20] Spalart, P. R., and Allmaras, S. R., "One-Equation Turbulence Model for Aerodynamic Flows," AIAA Paper 92-0439, Jan. 1992.

[21] Menter, F. R., "Zonal Two Equation k-ω Turbulence Models for Aerodynamic Flows," AIAA Paper 93-2906, July 1993.

[22] Dacles-Mariani, J., Zilliac, G. G., Chow, J. S., and Bradshaw, P., "Numerical/Experimental Study of a Wingtip Vortex in the Near Field," *AIAA Journal*, Vol. 33, No. 9, 1995, pp. 1561–1568.

[23] Lei, Z., "Effect of RANS Turbulence Models on Computational of Separated Flows over a Wing-Body Configuration," *Transactions of the Japan Society for Aeronautical and Space Sciences*, Vol. 48, Nov. 2005, pp. 150–160.

[24] Matsuo, Y., Nakamura, T., Tsuchiya, M., Ishizuka, T., Fujita, N., Ohkawa, H., Hirabayashi, Y., Takaki, R., Yoshida, M., Nakamura, K., Yamamoto, K., Suematsu, K., and Iwamiya, T., "Numerical Simulator III: Building a Terascale Distributed Parallel Computing Environment for Aerospace Science and Engineering," *Proceedings of the Parallel CFD 2002 Conference*, edited by Matsuno, K., Ecer, A., Satofuka, J., Periaux, J., and Fox, P., Elsevier Science B. V., Amsterdam, 2003, pp. 187–194.

[25] Ito, Y., and Nakahashi, K., "Direct Surface Triangulation Using Stereolithography Data," *AIAA Journal*, Vol. 40, No. 3, 2002, pp. 490–496.

[26] Ito, Y., and Nakahashi, K., "Surface Triangulation for Polygonal Models Based on CAD Data," *International Journal for Numerical Methods in Fluids*, Vol. 39, No. 1, 2002, pp. 75–96. doi:10.1002/fld.281

[27] Sharov, D., and Nakahashi, K., "Boundary Recovery Algorithm for Delaunay Tetrahedral Meshing," *Proceedings of 5th International Conference on Numerical Grid Generation in Computational Field Simulations*, edited by Soni, B. K., Thompson, J. F., Haeuser, J., and Eiseman, P. R., National Science Foundation Engineering Research Center for Computational Field Simulation at Mississippi State Univ., Mississippi State, MS, 1996, pp. 229–238.

[28] Ito, Y., and Nakahashi, K., "Improvements in the Reliability and Quality of Unstructured Hybrid Mesh Generation," *International Journal for Numerical Methods in Fluids*, Vol. 45, No. 1, May 2004, pp. 79–108. doi:10.1002/fld.669

[29] Ito, Y., Shih, A., Soni, B., and Nakahashi, K., "Approach to Generate High Quality Unstructured Hybrid Meshes," AIAA Paper 2006-0530, Jan. 2006.

[30] Tinoco, E. N., Venkatakrishnan, V., Winkler, C., and Mani, M., "Structured and Unstructured Solvers for the 3rd CFD Drag Prediction Workshop," AIAA Paper 2007-0255, Jan. 2007.

[31] Löhner, R., "Regridding Surface Triangulation," *Journal of Computational Physics*, Vol. 126, No. 1, 1996, pp. 1–10. doi:10.1006/jcph.1996.0115

[32] Mavriplis, D. J., "Grid Resolution Study of a Drag Prediction Workshop Configuration Using the NSU3D Unstructured Mesh Solver," AIAA Paper 2005-4729, June 2005.